A CFD-based method for slurry erosion prediction

Gianandrea Vittorio Messa, Stefano Malavasi

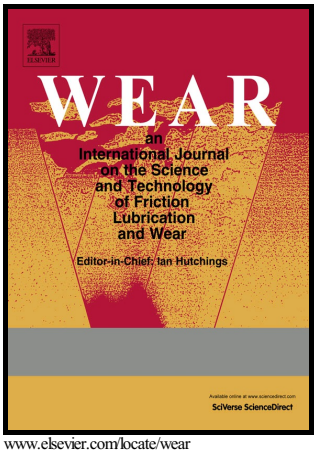

www.elsevier.com/locate/wear

PII: S0043-1648(17)31187-0
DOI: http://dx.doi.org/10.1016/j.wear.2017.11.025
Reference: WEA102307

To appear in: *Wear*

Received date: 27 July 2017
Revised date: 28 November 2017
Accepted date: 30 November 2017

Cite this article as: Gianandrea Vittorio Messa and Stefano Malavasi, A CFD-based method for slurry erosion prediction, *Wear* http://dx.doi.org/10.1016/j.wear.2017.11.025

A CFD-based method for slurry erosion prediction

Gianandrea Vittorio Messa, Stefano Malavasi

DICA, Politecnico di Milano, Piazza Leonardo da Vinci, 32, 20133 Milano, Italy

Abstract

The numerical prediction of the impact erosion produced by slurries is particularly challenging from the modeling point of view, not only due to the complex interactions between the phases, but also because self-induced geometry changes can influence the course of the wear process. The usual methodology for impact erosion estimation, which is based on the Eulerian-Lagrangian description of the slurry flow followed by the application of a single-particle erosion model to each particle-wall impingement, may be able to reproduce the complex physics underlying slurry erosion only at the price of complex algorithms and heavy computation, which is unaffordable in practical applications. In order to overcome these difficulties, an alternative approach was proposed, which involved the steady-state simulation of the slurry flow by an Euler-Euler model followed by the repeated calculation of individual particle trajectories in the proximity of the solid walls and the continuous update of the wear profile. The improved accuracy obtained in the simulation of several abrasive jet impingement experiments reported in the literature make the application of this method to more complex flows very promising.

Keywords: Abrasive jet testing, Computational fluid dynamics, Mixed Euler-Euler \ Euler-Lagrange approach, Impact wear, Slurry erosion

Nomenclature

A	Cell surface area (L^2)
$\tilde{A}$,$\tilde{B}$,$\tilde{C}$,$\tilde{D}$	coefficients in Eq. 8 (-)
B	width of the specimen (L)
C_1,C_2	coefficients in Eq. 12 (-)
C_d	drag coefficient (-)
C_l	lift coefficient (-)
C_M	solid mass fraction at nozzle exit (-)
C_μ	dimensionless parameter (-)
C_{vm}	virtual masss coefficient (-)
$\mathcal{D}$	component of $\dot{M}$ due to phase diffusion (MT^{-1})
d	nozzle diameter (L)
d_p	particle equivalent diameter (L)
d_p^+	dimensionless particle size (-)
E_C	cutting wear related term in Eq. 12 (M)
E_D	deformation wear related term in Eq. 12 (M)
E_p	mass removed by a single impact (M)

$\dot{E}$	erosion rate (MT^{-1})
$\dot{E}_{\mathrm{tot}}$	erosion rate of the whole wall boundary (MT^{-1})
ER_{int}	integral erosion ratio (-)
ER_{ref}	reference integral erosion ratio (-)
$\mathcal{F}$	component of $\dot{M}$ due to advection (MT^{-1})
F_s	particle shape related coefficient (-)
H	nozzle-to-specimen distance (L)
H_ν	Vickers hardness of target material ($\mathrm{ML}^{-1}\mathrm{T}^{-2}$)
I	turbulence intensity (-)
K	coefficient in Eq. 8 (-)
k	turbulent kinetic energy of the fluid phase ($\mathrm{L}^2\mathrm{T}^{-2}$)
k_s	turbulent kinetic energy of the solid phase ($\mathrm{L}^2\mathrm{T}^{-2}$)
L	length of the specimen (L)
l_e	eddy size (L)
$\dot{M}$	solid mass flux (MT^{-1})
$\mathcal{M}$	impinging solid mass flux (MT^{-1})
m_p	particle mass (M)

$\dot{m}_p$	particle mass flow rate (MT^{-1})
n	number of Lagrangian particles (-)
N_T	number of timesteps (-)
P	average pressure ($\mathrm{ML}^{-1}\mathrm{T}^{-2}$)
r	radial coordinate (L)
Δr	Cell size along radial direction (L)
Re_m	mixture Reynolds number, Eq.10 (-)
Re_p	particle Reynolds number (-)
s_s	friction factor of the solid phase (-)
T	testing time (T)
t	physical time (T)
$\tilde{t}$	Lagrangian time (T)
t_e	eddy lifetime (T)
t_r	particle transit-time (T)
Δt	timestep size (T)
U_{tsh}	threshold velocity for deformation wear (LT^{-1})
U_z	component of $\mathbf{U}$ along direction z (LT^{-1})

$\tilde{v}_{0,r}$	component of $\tilde{\mathbf{v}}_0$ along direction r (LT^{-1})
$\tilde{v}_{0,z}$	component of $\tilde{\mathbf{v}}_0$ along direction z (LT^{-1})
V_{jet}	jet velocity (LT^{-1})
V_r	component of $\mathbf{V}$ along direction r (LT^{-1})
V_z	component of $\mathbf{V}$ along direction z (LT^{-1})
W_p	particle volume (L^3)
y^+	dimensionless wall distance of near-wall nodes (-)
z	axial coordinate (L)
z'	coordinate in Figs. 9 and 15 (L)
Δz	Cell size along axial direction (L)
Greek Symbols	
β	coefficient in Eq. 11 (-)
δ	thickness of the Lagrangian layer (L)
ε	turbulence dissipation rate ($\mathrm{L}^2\mathrm{T}^{-3}$)
η	erosion depth (L)
$\dot{\eta}$	penetration rate (LT^{-1})
$\eta_{\max}$	maximum erosion depth (L)

$\theta_{p,w}$	particle impact angle (-)
μ	dynamic viscosity of the fluid phase ($\mathrm{ML^{-1}T^{-1}}$)
μ_m	friction, mixture viscosity-related parameter ($\mathrm{ML^{-1}T^{-1}}$)
μ_s	dynamic viscosity of the solid phase ($\mathrm{ML^{-1}T^{-1}}$)
μ_t	eddy viscosity of the fluid phase ($\mathrm{ML^{-1}T^{-1}}$)
$\mu_{t,s}$	eddy viscosity of the solid phase ($\mathrm{ML^{-1}T^{-1}}$)
ξ_r, ξ_z	random normal scalars (-)
ρ_f	fluid density ($\mathrm{ML^{-3}}$)
ρ_p	particle density ($\mathrm{ML^{-3}}$)
ρ_w	target material density ($\mathrm{ML^{-3}}$)
σ_ϕ	turbulent Schmidt number for volume fractions (-)
$\tau_{w,f}$	wall shear stress of the fluid phase ($\mathrm{ML^{-1}T^{-2}}$)
$\tau_{w,s}$	wall shear stress of the solid phase ($\mathrm{ML^{-1}T^{-2}}$)
Φ	average volume fraction of the solid phase (-)
ϕ'	fluctuating volume fraction of the solid phase (-)
φ	specimen shape correction factor (-)
ψ	particle spherical coefficient (-)

Vectors

$\mathbf{M}$	interfacial momentum transfer term ($\mathrm{ML^{-2}T^{-2}}$)
$\mathcal{N}$	vector of standard normal variables (-)
$\mathbf{n}$	unit normal vector (-)
$\mathbf{U}$	average velocity vector of the fluid phase ($\mathrm{LT^{-1}}$)
$\mathbf{u}$	velocity vector of the fluid phase ($\mathrm{LT^{-1}}$)
$\mathbf{u}'$	fluctuating velocity vector of the fluid phase ($\mathrm{LT^{-1}}$)
$\mathbf{V}$	average velocity vector of the solid phase ($\mathrm{LT^{-1}}$)
$\mathbf{V}^{//}$	component of $\mathbf{V}$ parallel to the wall at the near-wall nodes ($\mathrm{LT^{-1}}$)
$\mathbf{v}'$	fluctuating velocity vector of the solid phase ($\mathrm{LT^{-1}}$)
$\tilde{\mathbf{v}}$	particle velocity vector ($\mathrm{LT^{-1}}$)
$\tilde{\mathbf{v}}_0$	initial particle velocity vector ($\mathrm{LT^{-1}}$)
$\mathbf{v}_{p,w}$	particle impact velocity vector ($\mathrm{LT^{-1}}$)
$\tilde{\mathbf{x}}$	particle position vector (L)

Subscripts and superscripts

$*$	interpolated at the center of the interface element
$\langle ... \rangle$	average over all impingements

$\rightarrow j = 1...N_T$	within time interval $[(j-1)\Delta t, j\Delta t]$
$j = 1...N_T$	at time $j\Delta t$
T	at time T
@p	interpolated at particle position
el,i	of generic interface element
el,w	of generic wall element
in	at inlet section

1. Introduction

The erosion of the surfaces exposed to the impingements of solid particles in slurries is a very serious concern in many engineering fields, such as oil and gas and mining, as it causes downtime, loss of income and high repair costs. For some decades, the effort of researchers has been directed to the development of models for predicting the impact erosion, which, when applied by engineers, become a very useful tool for improving design and management procedures.

Erosion is traditionally estimated by means of single-particle erosion models, which treat the wear process in terms of the interaction between each abrasive particle and the target surface and express the mass of material removed by a particle hitting a surface, E_p, as a function of the particle mass, m_p, the modulus of the particle impact speed vector, $|\mathbf{v}_{p,w}|$, the parti-

cle impact angle, $\theta_{p,w}$, and some properties of the materials involved in the erosion process (Figure 1). A large number of single-particle erosion models have been proposed in the literature [1, 2], and, in most cases, they are empirical or semi-empirical algebraic expressions with the same mathematical structure. The fluid dynamic characteristics of the abrasives at the impact stage, i.e. $|\mathbf{v}_{p,w}|$ and $\theta_{p,w}$, are obtained by two-phase fluid-dynamic models based on the Eulerian-Lagrangian approach, in which the fluid flow is solved in an Eulerian framework and the solid phase is simulated by tracking the trajectories of a certain number of particles [3].

The above mentioned approach has been used, with different possible outcomes, to predict several gas-solid and liquid-solid erosion processes, from simple (i.e. abrasive jet impingement tests, as reviewed in [4]) to complex (i.e. those occurring in a valve [5–12]). However, its application to slurry erosion is particularly difficult because of two reasons.

First, the solid content of slurries is generally high enough for them to behave as dense. This means that the influence of the particles on the fluid flow (two-way coupling interactions) and particle-particle collisions and contacts (four-way coupling interactions) are important. Even if numerical techniques are available to handle these effects in an Eulerian-Lagrangian framework [13], the high computational cost results in the practical impossibility of applying them to many engineering systems. In support of this claim, it is noted that the few attempts in this direction concerned rather simple calculation domains or flows in which four-way coupled effects were limited to small regions of space [8, 14, 15]. Actually, peculiar features characterize the erosion produced by massive amounts of particles. For instance, a

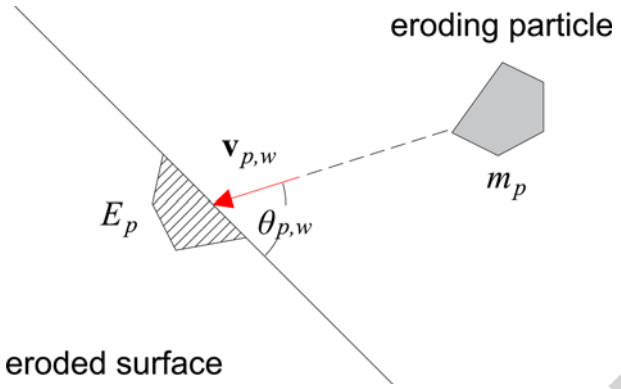

Figure 1: An eroding particle hitting a surface.

decrease in the integral erosion ratio, i.e. the ratio of the eroded mass to the mass of abrasives, with increasing solid concentration has been observed in several abrasive jet impingement experiments [16–22], and interpreted as a consequence of the protective action that the rebounding particles exert on the surface through their interaction with the incoming ones (shielding effect). Numerical simulations carried out by Mansouri et al. [21] and Mahdavi et al. [22] showed that, in case of dense flows, the application of a decoupled, steady-state Eulerian-Lagrangian model, in which the two- and four-way coupling interactions between the phases are neglected, produces erosion estimates in disagreement with the experimental evidence, besides being theoretically questionable.

Second, the changes in the flow field caused by the removal of material from the impinged surfaces are likely to play a significant role in slurry erosion. The paper of Nguyen et al. [23] demonstrated that, even for flows with low solid content, self-induced geometry changes can significantly affect the development of the erosion process in abrasive jet impingement tests, yield-

ing a decrease in the integral erosion ratio with time. At a different scale, the same effect was observed in abrasive slurry-jet micro-machining (ASJM) processes. In ASJM, a slurry jet consisting of water and particles is used to cut and mill a variety of materials, creating micro-channels and holes. In many ASJM experiments [24–28], the depth of micro-machined channels increased less-then-linearly with the number of machining passes. This behavior was interpreted as a consequence of the changes in the slurry flow field occurring as the channels become deeper. It is noted that, even if all the aforementioned studies refer to slurries with low solid content, the presence of high solid concentrations is likely to further enhance the importance of geometry changes, since dense slurries are expected to cause greater erosion depths for similar testing times.

Conventional CFD-based erosion modeling in oil and gas and mining applications assume a constant erosion rate and unchanging surface profile. Such hypothesis, which is reasonable for shallow erosion scars, can lead to inaccurate predictions for higher wear depths. This is evident from the already mentioned abrasive jet test results of Nguyen et al. [23], but it was also focus of discussion in the papers by Wallace et al. [7], McLaury et al. [29], and Wong et al. [30], concerning more complex flows. Similarly, Nouraei et al. [24] adapted for use in ASJM a surface evolution model initially developed for abrasive air jet micro-machining and assuming constant erosion rate in the centerline of the wear scar [31]. The authors reported good agreement with their ASJM experiments unless the aspect ratio of the machined channel (depth/width) exceeds a threshold value, thereby assessing the applicability of the model to shallow channels.

Relatively few attempts have been reported to account for geometry changes in erosion prediction models. Solnordal and Wong [32] proposed a particle-only model which assumes the motion of the particles to be completely driven by inertia and updates the wear profile based on changes in the impact locations and impact angles. Comparison with different experiments revealed the effectiveness of this approach for dilute gas-solid flows, where fluid-particle and particle-particle interactions can be ignored. The particle-only model was then successfully applied by Schrade et al. [33] to predict the erosive change of shape of the leading edge of compressor blades. Yaobao et al. [34] studied how the fluid dynamic characteristics of hydraulic spool valves are affected by solid particle erosion. The authors developed a predictive model in which the Eulerian-Lagrangian equations are repeatedly solved in a domain that is updated according to the development of the wear profile. The problem was modeled as two-dimensional axisymmetric, and the authors obtained good agreement between numerical predictions and experimental data regarding both a laboratory test and a field case. Rizkalla and Fletcher [35] proposed a computational model for slurry abrasion-erosion which takes self-induced geometry changes into account by iteratively solving the two-phase flow equations. Unlike all previous ones, in this study the slurry flow is simulated using an Euler-Euler model, in which both phases are interpreted as interpenetrating continua and solved in an Eulerian, cell-based framework [3]. The model was employed to predict the erosion of small converging-diverging channels and, after calibration of some model's constant, the authors reported good agreement with their experiments. They also underlined that the iterative update of the flow field is

necessary to achieve precise prediction of the amount of material removed by erosion. In a recent work [36], the authors of the present paper proposed a numerical strategy to account for self-induced geometry changes in the estimation of the erosion produced by a dilute slurry jet. The slurry flow was computed only once by a one-way coupled, steady-state Eulerian-Lagrangian model, and the evolution of the wear profile was obtained by integrating a simplified formulation of the particle Lagrangian equation of motion in the erosion hole. Finally, it is noted that surface evolution models accounting for geometry modifications have also been developed for application to ASJM. Haghbin et al. [26] applied empirical correction factors to a solution for shallow channels in order to extend its applicability to deeper channels. To the same purpose, Kowsari et al. [28] proposed two modeling strategies, the former involving a CFD simulation of the flow after each machining pass and the latter employing an approximate, empirically-calibrated model for the development of the stagnation zone.

In the present work, a numerical methodology was developed to attain improved prediction of slurry erosion with, at the same time, sufficiently low computational cost to be applicable to real-case geometries. As in [36], the slurry flow field was calculated only once, but an Euler-Euler model was used here to capture all the interactions between the phases occurring in dense flows without the need of resorting to computationally expensive four-way coupled Eulerian-Lagrangian models. A number of individual particles were then released close to the solid walls, and their trajectories were tracked by numerically solving a particle Lagrangian equation of motion unless they impinged against the boundary of the erosion hole. After applying a single-

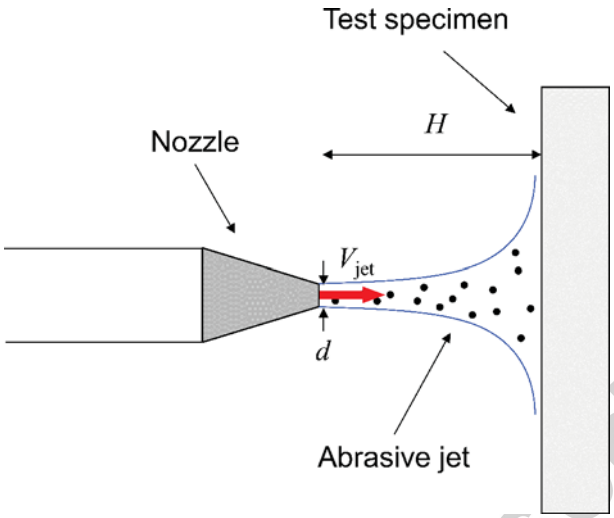

Figure 2: Sketch of a normal abrasive jet impingement test.

particle erosion model to each particle-wall impingement, the eroded surface was displaced and new trajectories were tracked, reiterating the process over the whole period of exposure to erosion. Specific assumptions regarding the slurry flow in the erosion hole (which did not require any calibration with respect to experimental data) avoided the need for repeated and time-consuming solution of the Euler-Euler equations.

The proposed methodology was applied to the already mentioned benchmark case of abrasive jet impingement test and, compared to the steady-state models commonly used in the engineering practice, it provided improved agreement with the experimental data obtained by several experiments [18, 22, 23, 37] for different flow conditions. As sketched in Fig. 2, a submerged slurry jet is normally directed to the eroding specimen in all test cases, which differ for the nozzle diameter, d, the nozzle-to-specimen distance, H, the jet velocity, V_{jet}, the particle characteristics (density, size,

and shape), the solid mass fraction at the nozzle exit, C_M, and the testing time, T. The significance of the selected experiments for validation purposes is evidenced by the wide range of variability of C_M (1% to 25%) and T (30 min to 6 h).

The remainder of this paper is divided in four sections, followed by the conclusions. The first one describes the Euler-Euler model employed for simulating the slurry flow, together with the computational domain, the boundary condition, and the solution strategy. The second one illustrates the developed methodology for estimating the dynamic evolution of the erosion process starting from the Euler-Euler solution. The third one focuses on the application of the methodology to reproduce abrasive jet impingement experiments reported in the literature, comparing the numerical predictions to the experimental data. Finally, a discussion of the obtained results is provided in the fourth section.

2. Mathematical models

2.1. The Euler-Euler model

As already mentioned, in the Euler-Euler models the flow of the ensemble of particles, referred to as "solid phase", is modeled in Eulerian framework and solved coupled with that of the carrier fluid phase. In the present work, use was made of the extension of the Inter-Phase Slip Algorithm (IPSA) of Spalding [38] to slurry flows developed by the authors in previous work [39, 40]. The flows were simulated as statistically steady. Therefore, the mass and momentum conservation equations for the fluid and the solid phases are, respectively,

$$\nabla \cdot [\rho_f (1-\Phi) \mathbf{U}] - \nabla \cdot \left(\rho_f \overline{\phi' \mathbf{u}'}\right) = 0 \tag{1}$$

$$\nabla \cdot (\Phi \rho_p \mathbf{V}) + \nabla \cdot \left(\rho_p \overline{\phi' \mathbf{v}'}\right) = 0 \tag{2}$$

$$\begin{aligned} &\nabla \cdot [\rho_f (1-\Phi) \mathbf{U}\mathbf{U}] - \nabla \cdot \left(\rho_f \overline{\phi' \mathbf{u}'} \mathbf{U}\right) \\ &- \nabla \cdot [(1-\Phi)(\mu + \mu_t) \nabla \mathbf{U}] = -(1-\Phi) \nabla P + \mathbf{M} \end{aligned} \tag{3}$$

$$\nabla \cdot (\rho_p \Phi \mathbf{V}\mathbf{V}) + \nabla \cdot \left(\rho_p \overline{\phi' \mathbf{v}'} \mathbf{V}\right) - \nabla \cdot [\Phi (\mu_s + \mu_{t,s}) \nabla \mathbf{V}] = -\Phi \nabla P - \mathbf{M} \tag{4}$$

where: ρ_f and ρ_p are the densities of the fluid and the particles, respectively; Φ and ϕ' are the local average and fluctuating volume fraction of the solid phase; $\mathbf{U}$, $\mathbf{u}'$, $\mathbf{V}$, and $\mathbf{v}'$ are the local average and fluctuating velocity vector of the fluid and solid phases, respectively; P is the average pressure, shared by the phases; μ, μ_s, μ_t, $\mu_{t,s}$ are the dynamic and eddy viscosities of the fluid and solid phases, respectively; and $\mathbf{M}$ is the interfacial momentum transfer term. The correlations between the fluctuating velocities and the fluctuating volume fractions are modeled by means of the eddy diffusivity hypothesis, as follows:

$$\overline{\phi' \mathbf{u}'} = \overline{\phi' \mathbf{v}'} = -\frac{\mu_t}{\rho_f \sigma_\phi} \nabla \Phi \tag{5}$$

in which σ_Φ is the turbulent Schmidt number for volume fraction, which is set to 0.7.

The dynamic viscosity of the solid phase, μ_s, accounting for the intergranular stresses among the particles, is evaluated by assuming a linear relationship between μ, μ_s, and the parameter μ_m, which will be defined later:

$$\mu_m = \mu (1-\Phi) + \mu_s \Phi \tag{6}$$

The interfacial momentum transfer term $\mathbf{M}$ quantifies the momentum transfer between the phases, and it includes drag, lift, and virtual mass forces:

$$\begin{aligned}\mathbf{M} =& \frac{3}{4d_p}\rho_f \Phi C_d |\mathbf{V}-\mathbf{U}| (\mathbf{V}-\mathbf{U}) + \frac{6}{\pi} C_l \rho_f \Phi (\mathbf{V}-\mathbf{U}) \times (\nabla \times \mathbf{U}) \\ &+ C_{vm}\rho_f \Phi \left[(\mathbf{V}\cdot\nabla)\mathbf{V} - (\mathbf{U}\cdot\nabla)\mathbf{U}\right]\end{aligned} \tag{7}$$

where d_p is the particle equivalent diameter (that is, the diameter of a sphere of equivalent volume), and C_d, C_l, and C_{vm} are the drag, lift, and virtual mass coefficients, respectively. Both C_l and C_{vm} were set to 0.5, whilst the drag coefficient has been evaluated by means of the following correlation, which, as explained below, can be regarded as a generalization of the Haider and Levenspiel formula [41] to multiple particles:

$$C_d = \frac{24}{\mathrm{Re}_m}\left(1 + \tilde{A}\mathrm{Re}_m^{\tilde{B}}\right) + \frac{\tilde{C}}{1+\dfrac{\tilde{D}}{\mathrm{Re}_m}} \tag{8}$$

where:

$$\tilde{A} = \exp\left(2.33 - 6.46\psi + 2.45\psi^2\right) \tag{9a}$$

$$\tilde{B} = 0.096 + 0.557\psi \tag{9b}$$

$$\tilde{C} = \exp\left(4.91 - 13.89\psi + 18.42\psi^2 - 10.26\psi^3\right) \tag{9c}$$

$$\tilde{D} = \exp\left(1.47 + 12.26\psi - 20.37\psi^2 + 15.89\psi^3\right) \tag{9d}$$

In the equation above, the symbol ψ stands for the particle spherical coefficient, i.e. the ratio of the surface area of a volume equivalent sphere to the surface area of the considered particle. In Messa and Malavasi [4], we proposed the following classification (which is adopted also in this work),

namely ψ equal to 0.66, 0.76, and 0.86 for fully-sharp, semi-rounded, and fully-rounded particles, respectively. One of the peculiar features of the Euler-Euler model employed lies in the fact that, in the drag coefficient correlation, the particle Reynolds number $\mathrm{Re}_p = \rho_f d_p |\mathbf{V} - \mathbf{U}|/\mu$ is replaced by a mixture Reynolds number, defined as

$$\mathrm{Re}_m = \frac{\rho_f d_p |\mathbf{V} - \mathbf{U}|}{\mu_m} \tag{10}$$

The parameter μ_m, already appearing in Eq. 6, lacks of a precise physical characterization, but it essentially accounts for the additional resistance that a particle faces due to the presence of other particles. In turn, the evaluation of μ_m is made by employing the following equation, analog of the comprehensive correlation proposed by Cheng and Law [42] for the viscosity of a mixture, and, for this reason, μ_m is referred to as friction, mixture-viscosity related parameter:

$$\mu_m = \mu \cdot \exp\left\{ \frac{2.5}{\beta} \left[\frac{1}{(1-\Phi)^{\beta}} - 1 \right] \right\} \tag{11}$$

where β is a numerical coefficient depending on the shape of the particles, which was suggested as 3.0 for sand grains. It is noted that, when $\Phi \to 0$, then $\mu_m \to \mu$ and, therefore, Re_m reduces to the usual particle Reynolds number, Re_p.

The eddy viscosity of the fluid, μ_t, is obtained by means a two-phase extension of the $k - \varepsilon$ RNG turbulence model for high Reynolds number flows of Yakhot et al. [43], which is available as option in the used CFD code [44]. The eddy viscosity of the solid phase, $\mu_{t,s}$, is evaluated from μ_t by means of the algebraic correlation proposed by Issa and Oliveira [45], that is $\mu_{t,s} = \mu_t \rho_p / \rho_f$.

The Euler-Euler model described above has been developed within the authors' research group to simulate the slurry flows encountered in hydro-transport processes. Extensive comparison against experiments have demonstrated that, with low computational burden, the model is capable in correctly predicting the main features of fully-suspended slurry flows in straight pipes and fittings [39, 40, 46]. However, despite relying on some physical basis, it is primarily semi-empirical and practical in nature. Past research has suggested that the evaluation of C_d with respect to Re_m is an effective way to reproduce the phenomena occurring in regions with moderate or high solid volume fraction, where two- and four-way coupling interactions between the phases are important. However, the meaning of the parameter μ_m is not completely clear. More generally, terms such as the viscosities and the pressure in the momentum equation of the solid phase are not yet provided a clear physical characterization, nor they are associated to a precise physical mechanism. Research is still going on in this direction. Due to its proven reliability and efficiency, the Euler-Euler model is used in this study for the calculation of the slurry flow field produced by the impinging jet. However, note that the proposed erosion prediction methodology may be extended for coupling with different two-phase models as well.

2.2. Erosion model

A single-particle erosion model was needed for estimating the loss of material starting from the solution of the Euler-Euler model. This was achieved based on the method explained in detail in Section 3.1. In this study, the mechanistic erosion model developed by Arabnejad and co-workers [47–49] was employed, referring to the formulation reported in [48]. The mechanistic

model attributes the loss of material produced by an impact, E_p, to cutting and deformation mechanisms, and the erosion equation is:

$$E_p = F_s \left(E_C + E_D \right) \tag{12}$$

where E_C and E_D are the mass of material removed due to cutting and deformation wear, respectively, and F_s is a numerical coefficient related to particle shape, being suggested to 1, 0.53, and 0.2 for sharp, nearly-rounded, and fully-rounded grains, respectively [50]. The terms E_C and E_D are calculated as:

$$E_C = \begin{cases} C_1 m_p \dfrac{|\mathbf{v}_{p,w}|^{2.41} \sin\theta_{p,w} \left[2K \cos\theta_{p,w} - \sin\theta_{p,w} \right]}{2K^2} & \text{if } \tan\theta_{p,w} < K \\ C_1 m_p \dfrac{|\mathbf{v}_{p,w}|^{2.41} \cos^2\theta_{p,w}}{2} & \text{otherwise} \end{cases} \tag{13}$$

and

$$E_D = \begin{cases} C_2 m_p \left(|\mathbf{v}_{p,w}| \sin\theta_{p,w} - U_{tsh} \right)^2 & \text{if} |\mathbf{v}_{p,w}| \sin\theta_{p,w} > U_{tsh} \\ 0 & \text{otherwise} \end{cases} \tag{14}$$

respectively. The parameters C_1, C_2, K, and U_{tsh} are empirical, material-dependent constants. Furthermore, U_{tsh} depends also on particle size, scaling with $d_p^{-3/2}$ [47]. It is noted that, according to Eq. 14, deformation wear occurs only if the component of the impact velocity normal to the wall exceeds the threshold value U_{tsh}.

2.3. Computational domain and boundary conditions

The axisymmetry of the geometry and the mean flow was exploited by solving only over a thin slice of the jet with one cell in the azimuthal direction. The computational domain is depicted in Fig. 3 together with the boundary conditions, which are inlet, outlet, solid walls, and axis of symmetry.

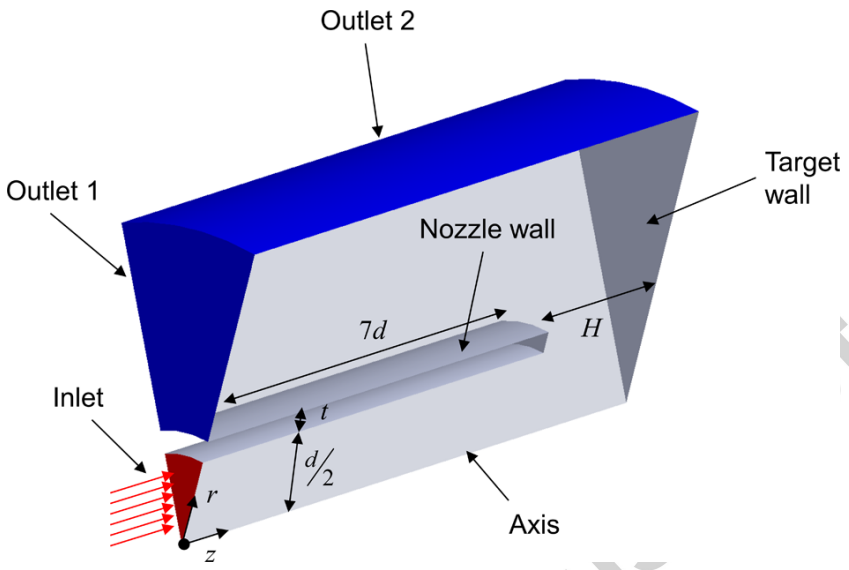

Figure 3: Computational domain and boundary conditions.

At the inlet, the mean axial velocities of both phases, U_z^{in} and V_z^{in}, the mean volume fraction of the solid phase, Φ^{in}, the turbulent kinetic energy of the fluid, k^{in}, and its dissipation rate, ε^{in}, are imposed. All these quantities were assumed uniformly distributed over the whole boundary, and calculated as follows: U_z^{in} and V_z^{in} were both set equal to the mean jet velocity; Φ^{in} was either the abradant volumetric concentration at the nozzle exit or that in the reservoir tank, according to the information provided by the experimenters; and k^{in} and ε^{in} were estimated as

$$k^{\text{in}} = \left(IU_z^{\text{in}}\right)^2 \tag{15}$$

and

$$\varepsilon^{\text{in}} = C_\mu^{3/4} \frac{\left(k^{\text{in}}\right)^{3/2}}{0.1d} \tag{16}$$

respectively, where $I = 0.05$ is the turbulence intensity, and $C_\mu = 0.0845$.

At the outlet boundaries, the mean pressure was specified as zero, and the normal gradients for all dependent variables are zero. The solid volume fraction and mass outflow of the solid phase result as part of the overall solution, but the solid phase was allowed to leave the domain only through a layer of the "Outlet 2" surface adjacent to the specimen, in order to avoid physically inconsistent Φ-distributions.

On the wall boundaries, the equilibrium log-law wall function [44] was employed to evaluate the average fluid velocity parallel to the wall at the first grid nodes, and the turbulent kinetic energy, and its dissipation rate in the near-wall cells. Specific tests showed that replacing the equilibrium log-law with its generalization to non-equilibrium conditions [44] produced no detectable changes in the erosion predictions.

In the lack of a well-established and universally accepted wall boundary condition for the solid phase in the Eulerian-Eulerian framework, use was made of the boundary condition proposed in Messa and Malavasi [40] and successfully validated for fully-suspended slurry flows in horizontal pipes. Such condition consists of imposing, in the near wall cells, a solid wall shear stress, $\tau_{w,s}$ equal to:

$$\tau_{w,s} = \rho_p s_s |\mathbf{V}^{//}| \mathbf{V}^{//} \tag{17}$$

where $\mathbf{V}^{//}$ is the average mean solid velocity parallel to the wall at the first grid node, and s_s is a friction factor of the solid phase. All the mathematical details of the boundary condition are reported in [40] and here only its basic idea is presented. Basically, s_s is differently calculated according to the local

dimensionless particle size, d_p^+, defined as:

$$d_p^+ = \frac{\rho_f d_p \sqrt{\tau_{w,f}/\rho_f}}{\mu} \tag{18}$$

where $\tau_{w,f}$ is the fluid wall shear stress. For $d_p^+ < 30$, s_s is calculated by a solid-phase analog of the equilibrium log-law wall function for smooth walls [44]. For $d_p^+ > 50$, s_s is evaluated by a local formulation of the semi-empirical correlation of Ferre and Shook for Bagnold's stress in the inertial regime of sheared annular flows [51], and calibrated using pressure-drop data for slurry flows in pipes. Within the intermediate range $30 < d_p^+ < 50$, the friction factor is a linear combination of the two expressions.

Finally, at the axis of symmetry, the normal gradients for all dependent variables are zero, so that a zero-flux condition is applied along such boundary.

2.4. Solution strategy

The commercial CFD code PHOENICS version 2014 was employed for the numerical solution of the finite volume analog of the mathematical model described above. This required adding user-defined functions and subroutines for implementation of specific constitutive equations and boundary conditions. The calculations were performed following the elliptic-staggered formulation in which volume fractions, scalar variables and pressure are stored at the grid nodes, whilst the velocities are stored at the cell faces. Simulation was steady-state, thereby converging to the steady-state solution without the need for the user to specify a timestep. Central differencing was employed for the diffusion terms, with harmonic averaging for diffusion coefficients, whilst the convection terms were discretized using the hybrid differencing scheme

of Spalding. In PHOENICS, the finite volume equations are solved iteratively by means of the SIMPLEST and IPSA algorithms of Spalding [38]. The calculation procedure is organized in a slab-by-slab manner along the z-direction, in which all the dependent variables are solved at the current slab before the routine moves to the next slab. The slabs are thus visited in turn, and the complete series of slab visits is referred to as a sweep through the solution domain. Multiple sweeps are required until convergence is attained, and the pressure equation is solved in a simultaneous whole-field manner at the end of each sweep. The settings related to the solution of the linear system of equations were the default ones in PHOENICS, which are well documented in [44].

The numerical solution procedure requires appropriate relaxation to the field variables to achieve convergence. To this purpose, use was made of the CONWIZ utility [44], in which the under-relaxation settings are automatically set by PHOENICS. The solver was run until the sum of the absolute residual errors on the whole solution domain is less than 0.01% of reference quantities determined by the code based on the total inflow of the variable in question. An additional requirement was that the values of the monitored dependent variables at a selected location do not change more than 0.001% between consecutive iteration cycles. The maximum number of sweeps was set to 10000, enough for attaining convergence for all testing cases.

The domain was discretized by means of a structured mesh in polar coordinates. The axisymmetry of the problem was exploited by setting one unit cell in the azimuthal direction, and, therefore, the computational grid was defined only in the $r - z$ plane. With the Euler-Euler model, mesh

requirements go beyond those for single-phase flow simulations, which are grid-independence and consistency with the wall treatment approach. In fact, the average process at the basis of the flow equations implies that the dimension of the computational cells must be representative of the local behavior of the ensemble of particles. The influence of the cell size on the erosion predictions was the objective of a detailed analysis, reported in Subsection 4.1. In the region between the nozzle exit and the target wall, the cells were square in shape with edges equal to $\sqrt{2}d_p$. Upstream the nozzle exit, where no high resolution is required and the number of cells has practically no effect on the wear results, in order to reduce the simulation time the mesh volumes were elongated along the z direction and their axial edges followed a power law distribution to avoid sudden changes in size. The overall number of mesh elements was dependent on both the geometrical characteristics of the nozzle-specimen system and the particle size, ranging from about 6000 to about 30000 for the different simulations.

The erosion calculations were performed by the in-house E-CODE, a MATLAB library developed within the authors' research group for wear estimation in complex geometries with multiple components. The methodology described in this paper was implemented in additional subroutines which expand the applicability of the library. Details about the followed solution procedure will be given in the next section.

3. Methodology for erosion prediction

The proposed strategy for attaining erosion estimates from the solution of the Euler-Euler model is described. Particularly, two separate sections

illustrate the key features, namely how to couple the fluid dynamic solution with a single-particle erosion model, and how to account for the self-induced geometry changes.

3.1. Coupling between Eulerian fluid-dynamic solution and single-particle erosion model

As already mentioned, the Euler-Euler model allows capturing all the interactions occurring in slurry flows avoiding the computational demand of four-way coupled Eulerian-Lagrangian simulations, which would be unaffordable for many engineering applications. However, for their inherent nature, single-particle erosion models are based on a Lagrangian framework and, therefore, their coupling with an Eulerian description of the solid phase is not straightforward. In order to overcome this issue, Messa et al. [52] introduced in the Euler-Euler domain a number of subdomains, in close position to the erosion hotspots, where a Lagrangian tracking of computational particles was performed and wear estimation could be obtained by employing single-particle erosion models. In this work, such mixed approach was taken to the limit by reducing the Lagrangian subdomain to a small layer adjacent to the entire wall boundary, referred to as "Lagrangian layer". The thickness of the Lagrangian layer, δ, does not have a precise physical meaning, and its value was assessed on the grounds of consistency analyses (that is, by demonstrating that further increase in δ did not produce appreciable changes in the erosion predictions). This will be discussed in Section 4.1.

For simplicity of exposure, and without loss of generality, the methodology will be illustrated making reference to a 2D case in the $r - z$ plane, shown in Fig. 4(a) and consistent with the computational domain in Fig. 3.

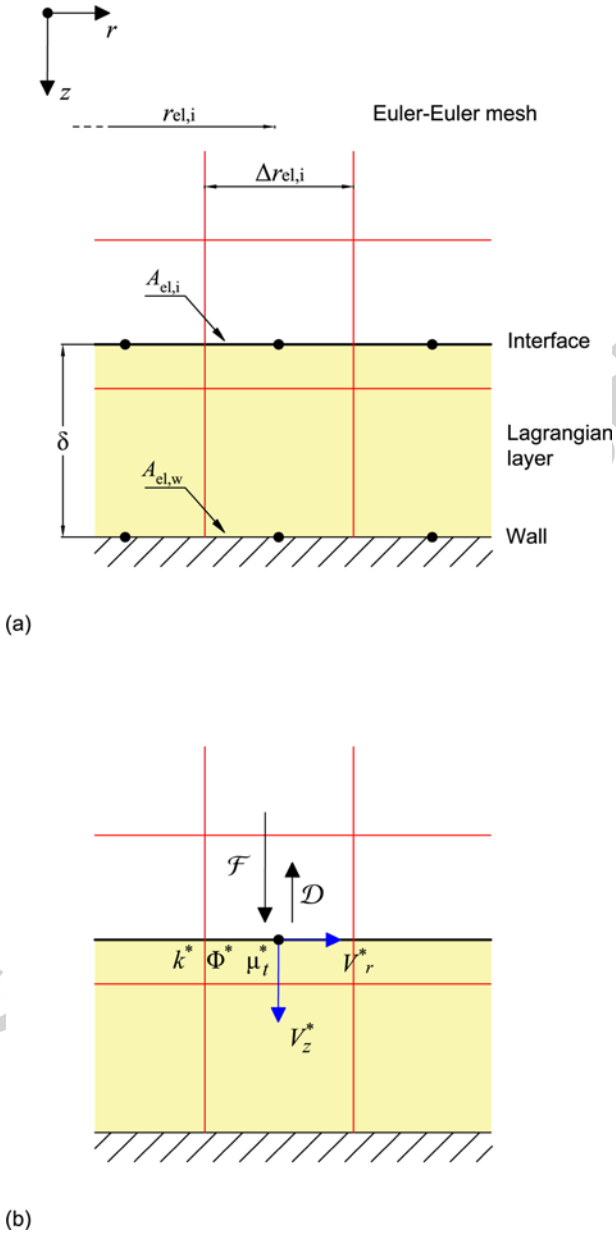

Figure 4: A simple two-dimensional case: (a) computational mesh, Lagrangian layer, and key geometrical parameters; (b) key fluid dynamic parameters

Two regular plane grids normal to the z direction are generated by projecting the CFD mesh on (i) the interface between the Lagrangian layer and the remainder of the domain and (ii) the wall boundary. Be $A_{\mathrm{el,i}}$ the surface area of a generic cell of the interfacial plane grid (for an axisymmetrical domain, $A_{\mathrm{el,i}} \approx 2\pi r_{\mathrm{el,i}} \Delta r_{\mathrm{el,i}}$). Computational particles were released from the cell, which acts as the inlet section in an Eulerian-Lagrangian simulation, and their trajectories were tracked within the Lagrangian layer. The number of particles released in the element, $n_{\mathrm{el,i}}$, was calculated as the ratio between a characteristic impinging solid mass flow rate through the cell, $\mathcal{M}_{\mathrm{el,i}}$, and the mass flow rate that each individual particle represents, $\dot{m}_p$.

Since the Euler-Euler model solves for the average fluid dynamic properties of the solid phase, the calculated solid mass flow rate through a surface in the proximity of a wall boundary can be interpreted as the net balance between that due to the impinging particles, directed towards the wall, and that due the rebounding particles, directed away from the wall. In principle, there is no way to separate the two contributions and identify the former, which is the only one that matters from the point of view of erosion. The solid mass flux through the interface cell is given by:

$$\dot{M}_{\mathrm{el,i}} = \underbrace{\Phi^* \rho_p V_z^* A_{\mathrm{el,i}}}_{\mathcal{F}_{\mathrm{el,i}}} \underbrace{- \rho_p \frac{\mu_t^*}{\rho_f \sigma_\phi} \frac{\partial \Phi}{\partial z}\bigg|^* A_{\mathrm{el,i}}}_{\mathcal{D}_{\mathrm{el,i}}} \tag{19}$$

where, as shown in Fig. 4(b), V_z is the component of the mean particle velocity vector along direction z, and the asterisk indicates that the quantities Φ, V_z, μ_t, and $\partial\Phi/\partial z$ are interpolated at the center of the cell. The two terms on the right hand side represent the solid mass flow rate due to advection and phase diffusion mechanisms, and are referred to as $\mathcal{F}_{\mathrm{el,i}}$ and $\mathcal{D}_{\mathrm{el,i}}$, respec-

tively. A positive value of V_z implies that $\mathcal{F}_{\mathrm{el,i}} > 0$, and, according to the notation in Fig. 4(b), it indicates the advective flux is directed towards the wall. However, the solid volume fraction increases as the wall is approached, yielding $\partial\Phi/\partial z > 0$ and, therefore, $\mathcal{D}_{\mathrm{el,i}} < 0$. Based on these considerations, the following criteria were adopted, namely (i) particles were released only from surface cells having $\mathcal{F}_{\mathrm{el,i}} + \mathcal{D}_{\mathrm{el,i}} > 0$, and (ii) in these cells, $\mathcal{M}_{\mathrm{el,i}}$ was assumed equal to $\mathcal{F}_{\mathrm{el,i}}$.

The initial positions of the $n_{\mathrm{el,i}} = \mathcal{M}_{\mathrm{el,i}}/\dot{m}_p$ particles were generated by random sampling over the cell's area, whilst their initial velocity, $\tilde{\mathbf{v}}_0$, includes mean and random fluctuating components, as follows

$$\tilde{v}_{0,r} = V_r^* + \xi_r \left(\frac{2k_s^*}{3}\right)^{1/2} \tag{20a}$$

$$\tilde{v}_{0,z} = V_z^* + \xi_z \left(\frac{2k_s^*}{3}\right)^{1/2} \tag{20b}$$

where: $\tilde{v}_{0,r}$ and $\tilde{v}_{0,z}$ are the components of $\tilde{\mathbf{v}}_0$ along directions r and z in Fig. 4, respectively; ξ_r and ξ_z are random scalars drawn from the standard probability density function (PDF); and V_r^* and k_s^* are the r-component of the local average velocity vector of the solid phase and the turbulent kinetic energy of the solid phase evaluated at the cell center by interpolation from the nearest nodes. The turbulent variable k_s, which is not calculated by the Euler-Euler model, was approximated with the corresponding fluid quantity, k.

The trajectory followed by each computational particle in the Lagrangian layer was determined by integrating the following ordinary differential equation:

$$\left(\rho_p + C_{vm}\rho_f\right) W_p \frac{\mathrm{d}\tilde{\mathbf{v}}}{\mathrm{d}\tilde{t}} = -\frac{1}{8}\pi\rho_f d_p^2 C_d |\tilde{\mathbf{v}} - \mathbf{u}_{@p}| \left(\tilde{\mathbf{v}} - \mathbf{u}_{@p}\right) - W_p \left(\nabla P\right)_{@p} \tag{21}$$

in conjunction with another one for particle position:

$$\frac{\mathrm{d}\tilde{\mathbf{x}}}{\mathrm{d}\tilde{t}} = \tilde{\mathbf{v}} \tag{22}$$

The symbols in Eqs. 21 and 22 are as follows: $\tilde{t}$ is the Lagrangian time, $\tilde{\mathbf{x}}$ and $\tilde{\mathbf{v}}$ are the instantaneous particle position and velocity vectors, W_p is the particle volume, and the subscript $@p$ indicates that the mean pressure gradient, ∇P, and the instantaneous fluid velocity vector, $\mathbf{u}$, are evaluated at particle position. The drag coefficient, C_d, was calculated from Eq. 8, with the particle Reynolds number based on μ_m, that is $\mathrm{Re}_m = \rho_f d_p |\tilde{\mathbf{v}} - \mathbf{u}_{@p}| \mu_{m,@p}$. As already noted, the use of the friction, mixture viscosity-related parameter $\mu_{m,@p}$, which depends on the local volume fraction, $\phi_{@p}$, is an empirical way to account for the effect of the surrounding slurry on the motion of the particles.

The vector $\mathbf{u}_{@p}$ was calculated as the sum of the mean fluid velocity at the same location, $\mathbf{U}_{@p}$, plus a fluctuation, $\mathbf{u}'$. In turn, $\mathbf{u}'$ was evaluated as:

$$\mathbf{u}' = \mathcal{N}\sqrt{\frac{2k_{@p}}{3}} \tag{23}$$

where $\mathcal{N}$ is a vector containing random scalars drawn from the standard PDF. The fluctuation $\mathbf{u}'$ was assumed to act over a time interval which is the minimum between (i) the eddy lifetime, $t_e = l_e/|\mathbf{u}'|$ and (ii) the particle transit-time, $t_r = l_e/|\mathbf{u}_{@p} - \tilde{\mathbf{v}}|$. In the above equations, l_e is the eddy size, estimated as:

$$l_e = C_\mu^{3/4} \frac{k_{@p}^{3/2}}{\varepsilon_{@p}} \tag{24}$$

As soon as this condition was not satisfied, a new fluctuation velocity was generated.

The particle motion equations (Eqs. 21-22) were integrated following the semi-analytical procedure described in Crowe et al. [53] until a particle left the Lagrangian layer, or reached a distance from the target wall equal to half of its size, in which case an impact occurs. Each impingement was associated to the center of the nearest element of the plane mesh in which the CFD mesh divides the wall boundary, whose surface area is denoted by $A_{\mathrm{el,w}}$ (Fig. 4(a)). The impact velocity, $\mathbf{v}_{p,w}$, was taken as the $\tilde{\mathbf{v}}$ vector half particle size from the wall, whilst the impact angle, $\theta_{p,w}$ was evaluated from the unit normal vector of the nearest element, $\mathbf{n}_{\mathrm{el,w}}$:

$$\mathbf{v}_{p,w} \cdot \mathbf{n}_{\mathrm{el,w}} = |\mathbf{v}_{p,w}| \cos\left(\frac{\pi}{2} - \theta_{p,w}\right) \tag{25}$$

The application of the single-particle erosion model (Eq. 12), in which the mass of the physical particle, m_p, was replaced by the mass flow rate of the computational particle, $\dot{m}_p$, yielded the mass flow rate of eroded material associated to the current impingement. The sum over the impingements occurring in the same wall element gave the erosion rate of this cell, that is $\dot{E}_{\mathrm{el,w}}$. Finally, the integral erosion ratio, ER_{int} [kg/kg] was obtained by summing the $\dot{E}_{\mathrm{el,w}}$ values over the elements and dividing by the solid mass flux entering the domain through the inlet section, $\dot{M}^{\mathrm{in}}$, as follows

$$ER_{\mathrm{int}} = \frac{\dot{E}_{\mathrm{tot}}}{\dot{M}^{\mathrm{in}}} = \frac{\dot{E}_{\mathrm{tot}}}{\rho_p V_z^{\mathrm{in}} \Phi^{\mathrm{in}} \left(\pi \frac{d^2}{4}\right)} \tag{26}$$

where $\dot{E}_{\mathrm{tot}} = \sum \dot{E}_{\mathrm{el,w}}$. Finally, the penetration rate of each element, i.e. the velocity at which the erosion depth increases, was calculated as:

$$\dot{\eta}_{\mathrm{el,w}} = \frac{\dot{E}_{\mathrm{el,w}}}{A_{\mathrm{el,w}} \rho_w} \tag{27}$$

where ρ_w is the density of the target material.

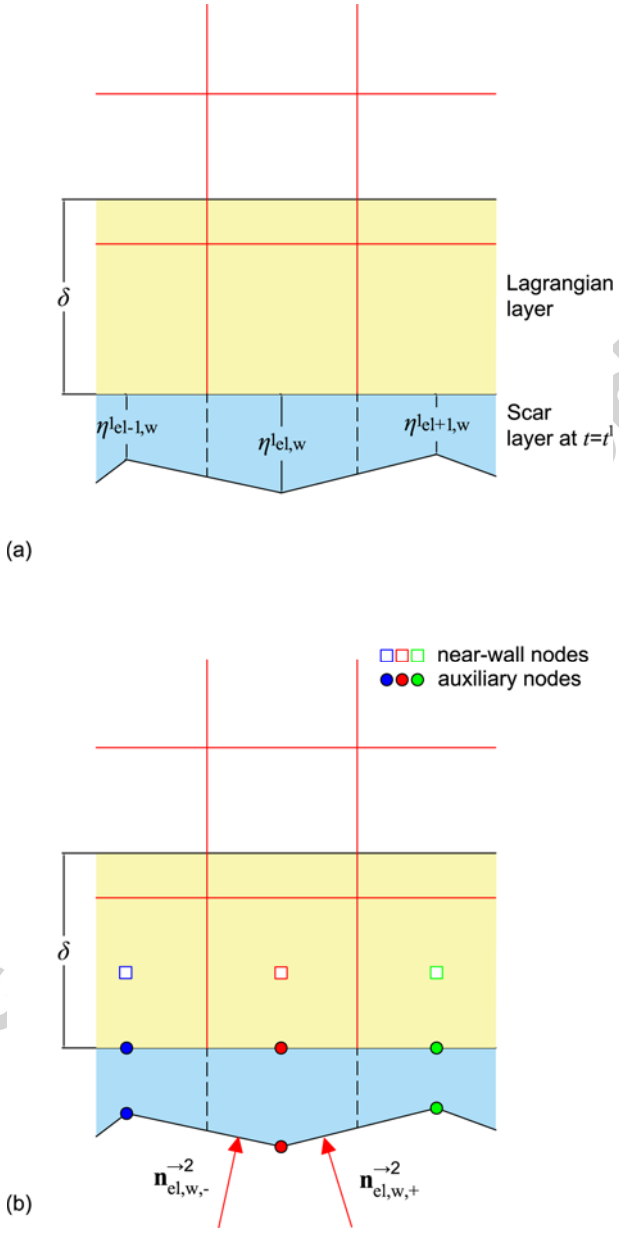

Figure 5: (a) subdomain in which the particles are tracked during the second timestep (b) auxiliary nodes for the evaluation of the slurry flow characteristics within the scar layer.

3.2. Dynamic evolution of the erosion process

The calculations described in subsection 3.1 provide time-independent wear parameters and, therefore, they predict a linear increase of erosion depth with time. In order to account for non-linear effects, the wear estimation procedure described above was executed within a time loop.

The time of exposure to erosion, T, was discretized in N_T intervals, which, for simplifying the discussion, were assumed equally-spaced with size Δt. The superscripts j and $\rightarrow j$ are used to denote quantities evaluated at the time instant $t^j = j\Delta t$ and within the time interval (t^{j-1}, t^j), respectively.

Following the steps described at the end of Subsection 3.1, the erosion rate of the generic element and the total erosion rate over the entire wall boundary were obtained within the interval $(0, t^1)$. These quantities, which are referred to as $\dot{E}^{\rightarrow 1}_{\mathrm{el,w}}$ and $\dot{E}^{\rightarrow 1}_{\mathrm{tot}}$ and correspond to the steady-state solution, were used to estimate the erosion characteristics at the end of the first timestep. Particularly, the integral erosion ratio, ER^1_{int}, and the erosion depth of each cell, $\eta^1_{\mathrm{el,w}}$ (Fig. 5(a)), were calculated by applying the following formulas:

$$ER^1_{\mathrm{int}} = \frac{\dot{E}^{\rightarrow 1}_{\mathrm{tot}} \Delta t}{\dot{M}^{\mathrm{in}} \Delta t} \tag{28}$$

$$\eta^1_{\mathrm{el,w}} = \dot{\eta}^{\rightarrow 1}_{\mathrm{el,w}} \Delta t = \frac{\dot{E}^{\rightarrow 1}_{\mathrm{el,w}} \Delta t}{A_{\mathrm{el,w}} \rho_w} \tag{29}$$

By connecting the local depths $\eta^1_{\mathrm{el,w}}$ and the wall boundary of the CFD domain, a new subdomain was generated, referred to as "scar layer" (Fig. 5(a)). Starting from the same initial conditions, the particles' trajectories were recalculated within the Lagrangian and the scar layers, unless they either left

the domain or impingements occurred. The integration of Eqs. 21 and 22 requires knowledge of the fluid dynamic variables $\mathbf{U}$, k, P, and Φ in the scar layer. However, these quantities cannot be directly determined from the Euler-Euler equations, which are solved only once and within the domain with unchanged geometry. Thus, they had to be modeled. In this work, the fluid was assumed still in the scar layer (that is, $\mathbf{U} = 0$ and $k = 0$), whilst the scalar variables P and Φ at particle's position were obtained by linear interpolation of the values at auxiliary nodes (filled circles in Fig. 5(b)), which, in turn, were equal to those at the closest near-wall nodes (unfilled squares in the same figure). This simple assumption procured slurry jet erosion predictions in reasonable agreement with the experimental evidence. Indeed, different slurry flow models can be employed in the context of the proposed approach, for this and other types of flows.

The impact velocities within the second timestep, $\mathbf{v}_{p,w}^{\rightarrow 2}$, were evaluated at half particle size from the crater, and the corresponding impact angles, $\theta_{p,w}^{\rightarrow 2}$, were obtained by applying Eq 25 with updated velocities and normal unit vectors. As clearly shown in Fig. 5(b), two different vectors ($\mathbf{n}_{\mathrm{el,w},-}^{\rightarrow 2}$ and $\mathbf{n}_{\mathrm{el,w},+}^{\rightarrow 2}$) are associated with the same element in a two-dimensional case.

The single-particle erosion model allowed obtaining the eroded mass flow rate of each impact, and, thus, the erosion rate of each element and the whole boundary between t^1 and t^2, i.e. $\dot{E}_{\mathrm{el,w}}^{\rightarrow 2}$ and $\dot{E}_{\mathrm{tot}}^{\rightarrow 2}$. The integral erosion ratio and the local erosion depth at t^2 were calculated as

$$ER_{\mathrm{int}}^2 = \frac{\dot{E}_{\mathrm{tot}}^{\rightarrow 1}\Delta t + \dot{E}_{\mathrm{tot}}^{\rightarrow 2}\Delta t}{\dot{M}^{\mathrm{in}} 2\Delta t} = \frac{1}{\dot{M}^{\mathrm{in}}}\frac{\dot{E}_{\mathrm{tot}}^{\rightarrow 1} + \dot{E}_{\mathrm{tot}}^{\rightarrow 2}}{2} \tag{30}$$

$$\eta^{2}_{\mathrm{el,w}} = \eta^{1}_{\mathrm{el,w}} + \dot{\eta}^{\rightarrow 2}_{\mathrm{el,w}} \Delta t = \eta^{1}_{\mathrm{el,w}} + \frac{\dot{E}^{\rightarrow 2}_{\mathrm{el,w}} \Delta t}{A_{\mathrm{el,w}} \rho_w} \tag{31}$$

The procedure above was repeated for all the subsequent timesteps $j = 3, ...N_T$, as follows: (i) identification of the scar layer at current timestep; (ii) particle tracking within the current domain (that is, Lagrangian layer and current scar layer); (iii) evaluation of the impact velocities, $\mathbf{v}^{\rightarrow j}_{p,w}$, and impact angles, $\theta^{\rightarrow j}_{p,w}$, based on the updated normal unit vectors, $\mathbf{n}^{\rightarrow j}_{\mathrm{el,w}}$; (iv) application of the single-particle erosion model to estimate the eroded mass flow rate of the impacts and subsequent calculation of the erosion rates of the elements and the entire target wall, $\dot{E}^{\rightarrow j}_{\mathrm{el,w}}$ and $\dot{E}^{\rightarrow j}_{\mathrm{tot}}$; (v) evaluation of the integral erosion rate and the erosion depth of each element by application of the following formulas:

$$ER^{j}_{\mathrm{int}} = \frac{\sum_{s=1}^{j} \dot{E}^{\rightarrow s}_{\mathrm{tot}} \Delta t}{\dot{M}^{\mathrm{in}} j \Delta t} = \frac{1}{\dot{M}^{\mathrm{in}}} \frac{\sum_{s=1}^{j} \dot{E}^{\rightarrow s}_{\mathrm{tot}}}{j} \tag{32}$$

$$\eta^{j}_{\mathrm{el,w}} = \eta^{j-1}_{\mathrm{el,w}} + \dot{\eta}^{\rightarrow j}_{\mathrm{el,w}} \Delta t = \eta^{j-1}_{\mathrm{el,w}} + \frac{\dot{E}^{\rightarrow j}_{\mathrm{el,w}} \Delta t}{A_{\mathrm{el,w}} \rho_w} \tag{33}$$

Finally, it is remarked that, whilst the Lagrangian layer does not change during the computation, the scar layer expands at each timestep depending on its configuration at the previous timestep. As it will be shown in the next section, both the Euler-Euler solution and the erosion model contribute to this evolutionary process.

4. Testing and validation of the methodology

The calculation method described in the previous section was validated against the outcomes of abrasive jet impingement experiments reported in

the literature by different researchers [18, 22, 23, 37]. Six cases were selected to assess the capability of the methodology in different testing conditions, reported in Table 1. All experiments were performed in closed loops in which the slurry is recirculated, and the integral erosion ratio was calculated by the experimenters as the ratio between the mass loss of test specimen, obtained by high precision balances, and the sand throughput, i.e. the product of the solid mass flow rate exiting the nozzle and the testing time. This, in turn, required to evaluate the concentration of the particles coming out of the nozzle. Another measured variable was the slurry flow rate, from which the jet velocity can be inferred. In some cases, the experimenters also used 3-D profilometers to measure the depth of erosion area.

The rectangular section of the specimens used in the experiments was taken into account when evaluating the integral erosion ratio from the axisymmetric solution. This was achieved by multiplying the erosion rate of each wall element, $\dot{E}_{\mathrm{el,w}}$, by a correction factor, $\varphi_{\mathrm{el,w}}$, given by:

$$\varphi_{\mathrm{el,w}} = \begin{cases} 1 & \text{if } r_{\mathrm{el,w}} \leq \dfrac{B}{2} \\ \dfrac{2}{\pi}\mathrm{asin}\left(\dfrac{B/2}{r_{\mathrm{el,w}}}\right) & \text{if } \dfrac{B}{2} < r_{\mathrm{el,w}} \leq \dfrac{L}{2} \\ \dfrac{2}{\pi}\left[\mathrm{asin}\left(\dfrac{B/2}{r_{\mathrm{el,w}}}\right) - \mathrm{acos}\left(\dfrac{L/2}{r_{\mathrm{el,w}}}\right)\right] & \text{if } \dfrac{L}{2} < r_{\mathrm{el,w}} \leq \dfrac{1}{2}\sqrt{L^2+B^2} \\ 0 & \text{if } r_{\mathrm{el,w}} > \dfrac{1}{2}\sqrt{L^2+B^2} \end{cases} \tag{34}$$

where B and L are the lengths of the edges of the rectangular specimen, and $r_{\mathrm{el,w}}$ is the radial position of the center of the current wall element. The sketch in Fig. 6 helps in understanding the criterion at the basis of the definition of the $\varphi_{\mathrm{el,w}}$ factor. It is noted that the formula for $\varphi_{\mathrm{el,w}}$ is approximate, as it should be derived from a ratio between areas rather than angles; furthermore,

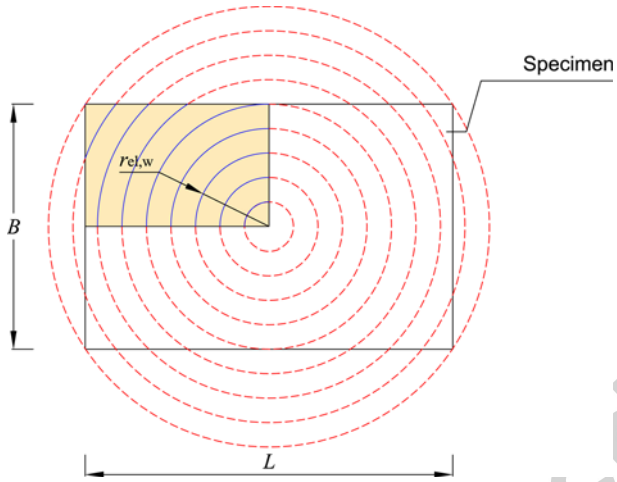

Figure 6: Procedure for estimating the erosion of a rectangular section specimen from the axisymmetric solution. The correction factor $\varphi_{\mathrm{el,w}}$ is the ratio between the angle spanned by the arcs lying in a quarter of the specimen (blue colored) and the right angle.

it assumes that the center of the specimen is perfectly aligned with the nozzle axis, which may not be the case in the actual experiments.

As a preliminary step, the numerical consistency of the solution was assessed.

4.1. Consistency of the erosion predictions

The post-processing procedure introduces some numerical settings which may have spurious effects on the wear estimates, namely the number of released particles, n, the number of time steps, N_T, and the thickness of the Lagrangian layer, δ. The consistency study of the numerical solution concerned these parameters in addition to the usual ones of CFD studies, namely grid size, convergence criterion, and so on. The fact that all these effects interact with each other increased the complexity of the analysis.

Case	Ref.	B [mm]	L [mm]	d [mm]	H [mm]	V_{jet} [m/s]	Target	ρ_w [kg/m^3]	H_ν [GPa]	ψ [-]	ρ_p [kg/m^3]	d_p [μm]	C_M [%]	T [h]
A	[23]	25	25	6.4	12.7	30	SUS304	7929	1.96	0.66	3940	150	1.32	0.5
B	[37]	25	37.5	8	12.7	14	SS316	7990	1.5	0.66	2650	300	0.6	6
C	[37]	25	37.5	8	12.7	14	SS316	7990	1.5	0.76	2650	150	0.6	6
D	[22]	51.92	77.29	7	12.7	13.7	SS316	8000	1.83	0.66	2650	300	$1 \div 18$	0.5
E	[22]	51.92	77.29	7	12.7	10.7	SS316	8000	1.83	0.66	2650	300	$1 \div 25$	0.5
F	[18]	19	32	4.8	9	8.8	44W	7833	1.60	0.76	2650	300	$1 \div 8$	2

Table 1: Testing conditions considered for comparison. In cases B to E, the dimensions of the section of the specimen, B and L, were obtained from the sketches of the CFD setup reported in Refs. [37] (cases B and C) and [54] (cases D and E)

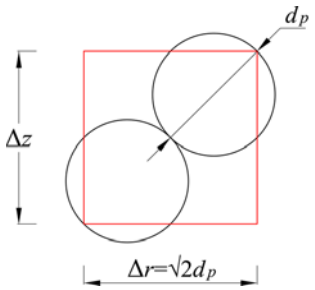

Figure 7: Minimum cell size in the consistency study.

Simulations aimed at consistency assessment were performed for all test cases and different erosion parameters were considered. Due to reasons of space, only few results regarding case A are presented herein. The employed values of the numerical constants in the erosion model were those suggested for SS316, namely $C_1 = 4.58 \cdot 10^{-8}$, $C_2 = 5.56 \cdot 10^{-8}$, $K = 0.4$, and $U_{tsh} = 5.8$ m/s, whilst the particle shape factor, F_s was set to 1. As already mentioned, the computational mesh consisted of square elements in the r-z plane, whose dimension $\Delta r = \Delta z$ was defined in compliance with the constraint imposed by the Euler-Euler models that the cell size must be representative of an ensemble of particles. Particularly, the smallest value was $\sqrt{2}d_p$, so that roughly two spherical particles fit into a grid cell (Fig. 7), the others were $2d_p$ and $3d_p$. It is noted that, in the selection of the testing cases, the requirements of the wall-function approach on which the Euler-Euler model is based were also taken into account. This was achieved by referring only to sufficiently large particles, which produced average y^+ values on the target wall between 30 and 130. The parameters n, N_T, and δ were varied between 100 and 10000, 1 and 40, and 1 and 3.5 times the cell

size, respectively.

The combined effect of n and N_T was studied first, and the results are shown in Figs. 8(a) and (b). The influence of the number of tracked particles was substantially negligible in terms of integral erosion ratio, but about 5000 trajectories were needed to attain a smooth erosion depth profile, which showed the typical "W" produced by slurry jets. Conversely, the integral erosion ratio was affected by the number of timesteps, but the series reached a plateau for $N_T \geq 15$. The influence of grid size and δ is shown in Fig. 8(c) for $n = 5000$ and $N_T = 15$. The Lagrangian layer had to extend over about three rows of cells for the integral erosion ratio at $t = T$ to be unaffected by further increase in δ. However, no independence was reached with respect to the grid resolution, being apparently impossible to meet the requirements of numerical accuracy and meaningfulness of the average. Following previous studies [55], a cell size of $\sqrt{2}d_p$ was judged the best compromise to overcome this typical issue of Euler-Euler models. In summary, the following settings were chosen, namely $n = 5000$, $N_T = 15$, $\delta = 3\Delta z$, and $\Delta z = \sqrt{2}d_p$. More extended analyses confirmed the suitability of these values for all simulation scenarios in Table 1. Finally, releasing the particles within the third row of cells from the wall (δ=3Δz) has also the advantage of reducing the dependence of the wear estimates on the wall boundary condition of the solid phase. As already noted, this is still an unresolved issue in Euler-Euler models.

4.2. Experiments by Nguyen et al. [23]

Nguyen et al. [23], who tested experimentally case A, reported values of the integral erosion ratio at different times during the test, namely 0.5, 5, 15, and 30 minutes. As already mentioned, the authors attributed the decrease

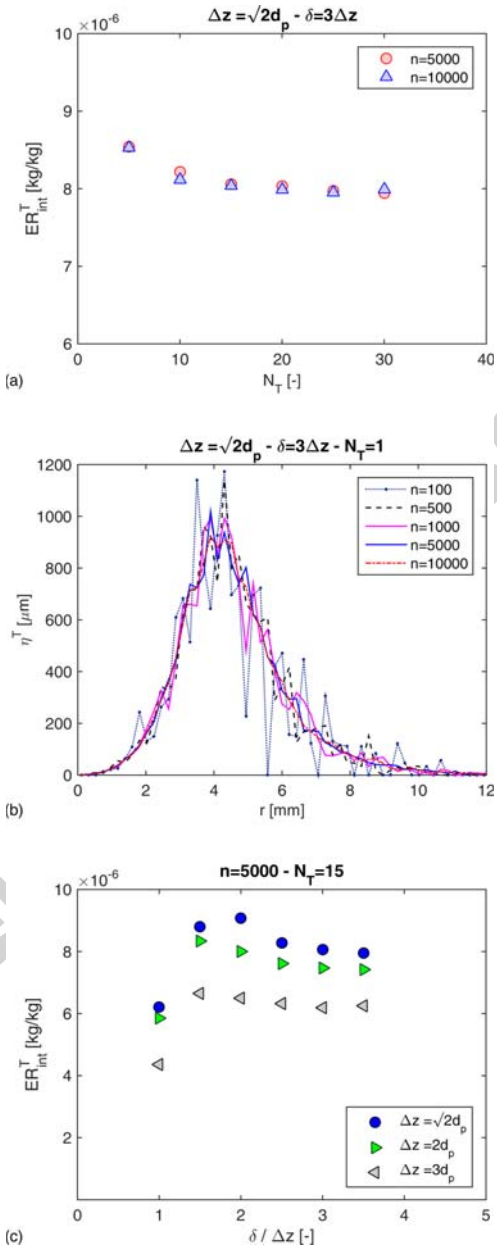

Figure 8: Consistency analysis of the wear estimates for case A.

of the integral erosion ratio with time to the geometry changes induced by the erosion process. The low solid concentration (1.32% by mass) suggests a limited importance of four-way coupling effects.

Details of the Euler-Euler solution are shown in Fig. 9. Particularly, the four plots report the distributions of $|\mathbf{U}|$, $|\mathbf{V}|$, P, and Φ downstream the nozzle outlet up to a distance from the target wall equal to $d_p/2$ (where the coordinate z', opposite to the z-direction, is zero). Such fluid-dynamic solution is consistent with those previously obtained using Eulerian-Lagrangian models [4, 23]. The slurry jet leaving the nozzle rapidly decelerates in the proximity of the wall, and, after impingement, it radially deflects. The deceleration of the jet is accompanied by an increase in pressure, which reaches the maximum value in correspondence to the stagnation point. The two phases move with similar velocity in the core region of the jet, but, mainly due to their different inertia, noticeable differences exist close to the stagnation region. The solid phase keeps uniformly distributed up to a small distance from the wall, then a sudden increase in mean solid volume fraction occurs in the stagnation region.

The predicted integral erosion ratio at the first timestep (which, as already noted, corresponds to the steady-state value) was $1.97 \cdot 10^{-5}$ kg/kg, about 40% lower than the measurement ($3.38 \cdot 10^{-5}$ kg/kg). However, as shown in Fig. 10(a), the time evolution of the normalized integral erosion ratio, obtained by dividing the integral erosion ratio by the value at the smallest measured/computed time, was in good agreement with the experimental data.

The predicted time evolution of the entire wear profile and the maxi-

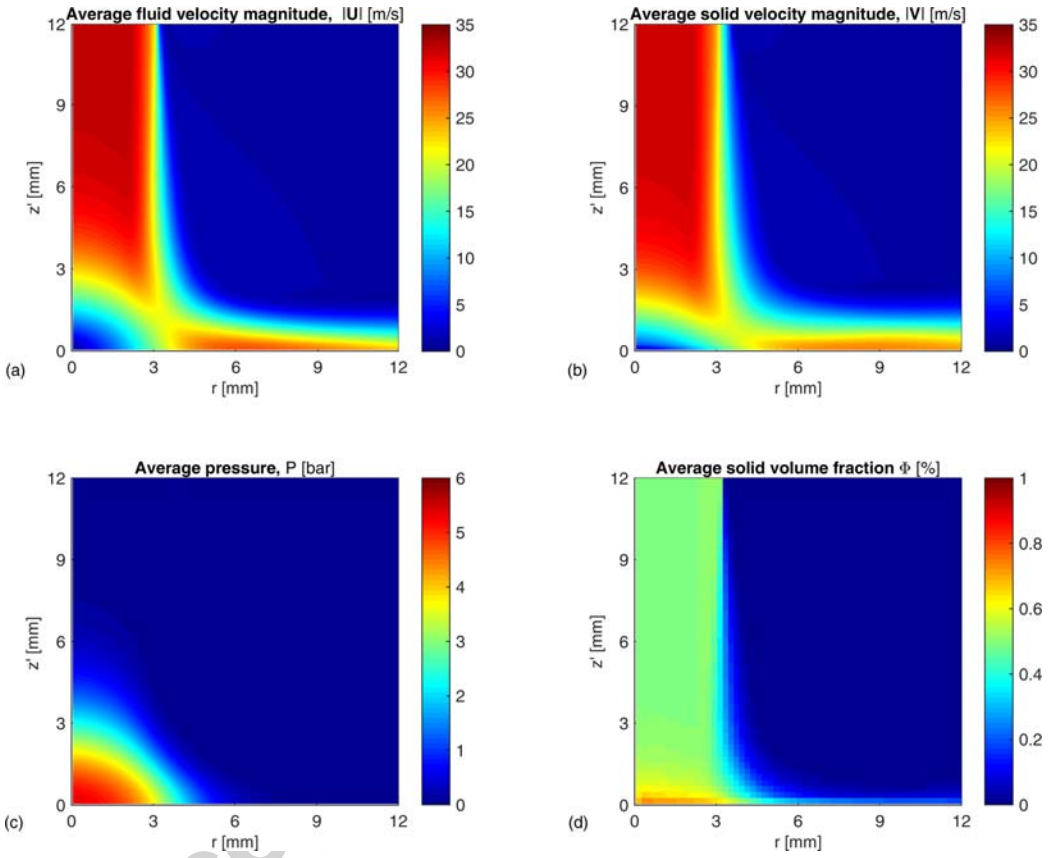

Figure 9: Detail of the Euler-Euler solution for case A: color plot distributions of (a) modulus of average velocity of the fluid phase; (b) modulus of average velocity of the solid phase; (c) average pressure; (d) mean solid volume fraction. The zero value of the coordinate z', opposite to the the z-direction, corresponds to a distance from the target wall equal to $d_p/2$.

mum erosion depth, shown in Figs. 10(b) and 10(c), respectively, revealed a correspondence between the reduction of the integral erosion ratio and the deceleration in the growth of the erosion hole. The proposed methodology was capable in reproducing this effect because, in order to reach the surface of the specimen and produce damage, the particles had to overcome the resistance exerted by the still fluid in the scar layer. As the time increased and the scar got deeper, the particle faced more and more difficulties in crossing the scar layer and, therefore, they impinged the target at lower velocity or even did not impinge it at all. As a consequence, the erosion slowed down. This is further exemplified in Fig. 10(d), which shows the time evolution of the mean particle impact velocity modulus, $\langle|\mathbf{v}_{p,w}|\rangle$ (that is, the average over all impingements). The curve indicates that, for case A, the model achieved a deceleration of the erosion process through a reduction of the impact velocity. No substantial variation was observed in the number of impingements and only minor changes occurred in the average impact angle. The plots in Fig. 10 underline the difference between the proposed methodology and the steady-state model, which predicts a constant growth of the wear depth in time.

Finally, Fig. 10(a) reports also the normalized integral erosion ratios as numerically predicted by Nguyen et al. [23]. These results were obtained by performing four independent, Eulerian-Lagrangian, two-way coupled simulations in which the experimentally-determined scar profile was imposed as domain boundary. This additional comparison further enhances the engineering potential of the proposed method, which evaluates the evolution of erosion starting from just one steady-state CFD simulation.

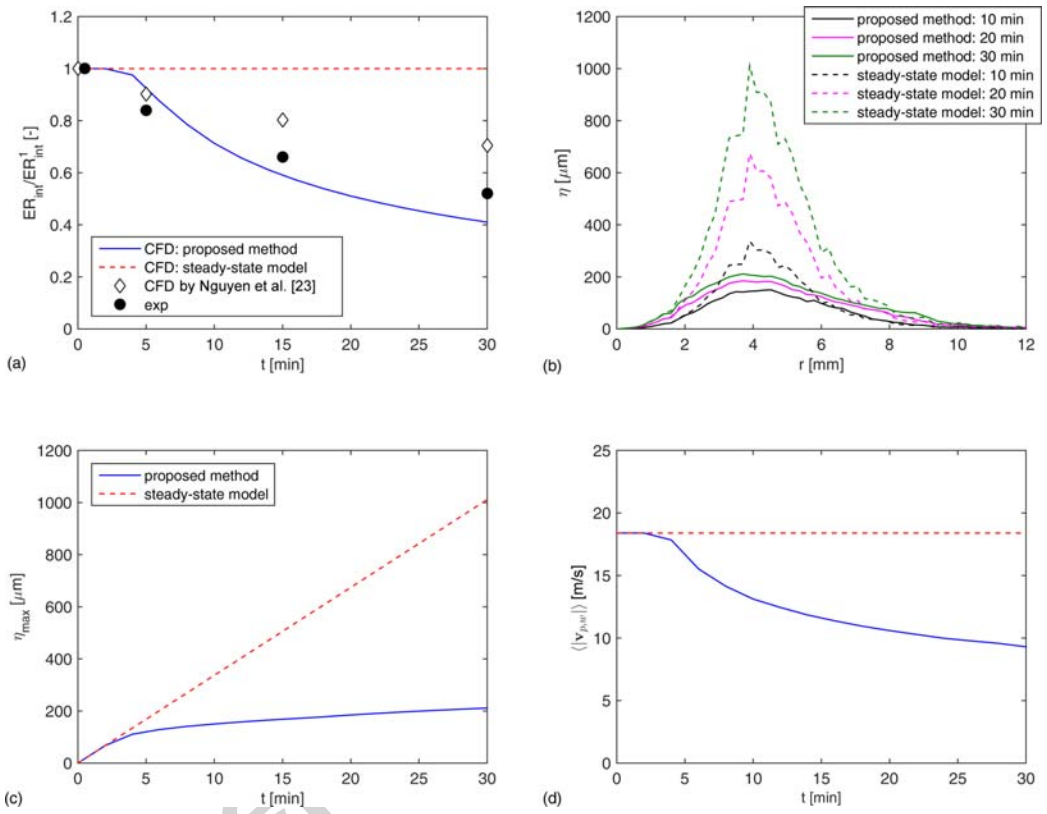

Figure 10: Comparison between proposed method and steady-state model for case A: (a) time evolution of the integral erosion ratio, normalized by the value at the smallest time; (b) erosion depth profiles at different timesteps; (c) time evolution of the maximum erosion depth, $\eta_{\max}$; (d) time evolution of the mean particle impact velocity modulus, $\langle |\mathbf{v}_{p,w}| \rangle$. Plot (a) reports also the experimental data and the CFD predictions of Nguyen et al. [23].

4.3. Experiments by Mansouri et al. [37]

Cases B and C, reported in Mansouri et al. [37], were characterized by different geometrical characteristics of the abrasive grains. In case B, the abradant was California 60 sand, with mean size of 300 μm and angular shape (thus, $\psi = 0.66$ and $F_s = 1$). In experiment C, Oklahoma #1 particles were used, with $d_p = 150$ μm and semi-rounded shape (thus, $\psi = 0.76$ and $F_s = 0.53$). All other test parameters, including particle density (2650 kg/m^3), were the same. The parameter U_{tsh} in the mechanistic erosion model was set to 2.0 m/s and 5.8 m/s for cases B and C, respectively. All other constants were not changed from the values reported in the previous section.

For both scenarios, the solution of the Euler-Euler model was qualitatively analogous to case A, depicted in Fig. 9. Similarly, the predicted integral erosion ratio decreased with time, as shown in Fig. 11(a). This trend corresponds to a deceleration in the growth of the wear depth, evident in Figs. 11(b) to (d). The behavior can be interpreted on the grounds of the considerations set up in Section 4.2.

The predicted erosion depth profiles at the end of the test were consistent with the experimental evidence, and so is the integral erosion ratio for case C, depicted in Fig. 11(b). Making a comparison against the experiment was more complicated for case B, because the numerical estimation was close to the integral erosion ratio obtained by integrating the measured wear depth profile, but this apparently did not match the value obtained by the experimenters by weighting the sample. Anyway, the simulation results appeared satisfactory.

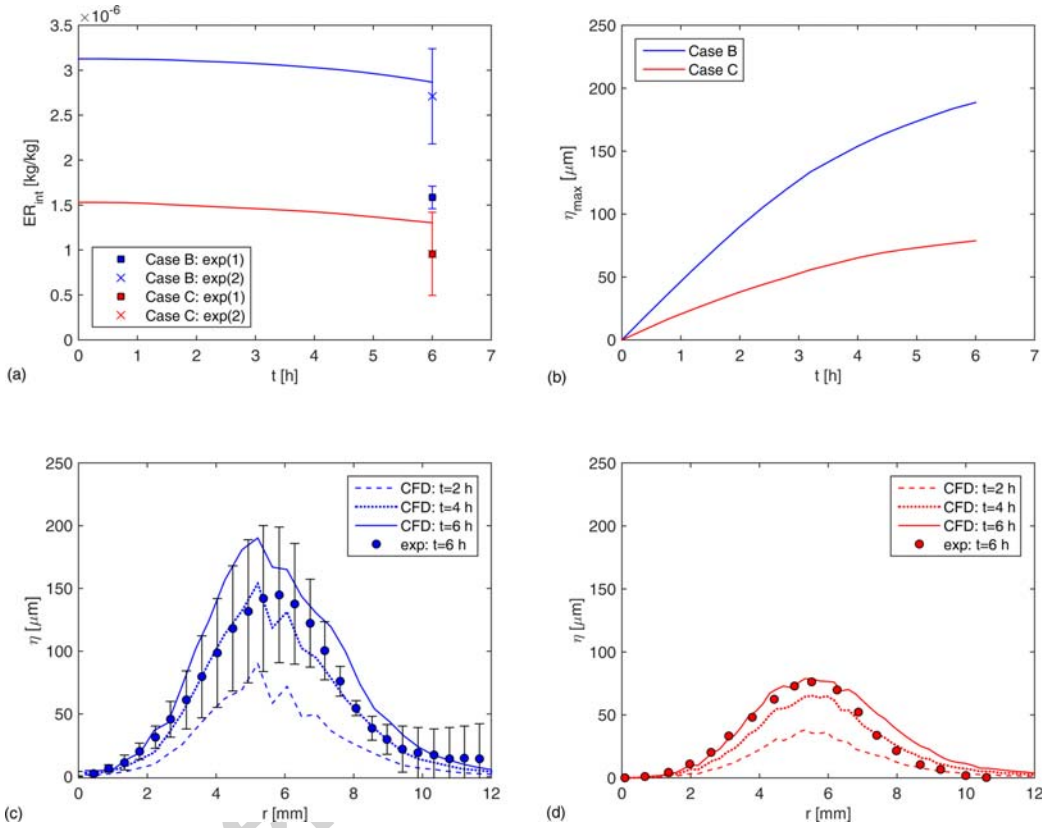

Figure 11: Results for cases B and C: (a) time evolution of the integral erosion ratio. Labels exp(1) and exp(2) stand for the integral erosion ratios reported by the Mansouri et al. [37] and obtained by integrating the experimentally determined scar profiles in plots (c) and (d), respectively; (b) time evolution of the maximum erosion depth; (c,d) time evolution of the wear depth profile and comparison against the experimental measurements.

4.4. Experiments by Mahdavi et al. [22]

In experiments D and E, performed by Mahdavi et al. [22], the solid concentration was increased without varying the testing time, making them interesting validation cases for a couple of reasons. On one hand, the considerable levels of concentration (up to about 25% by mass) suggested that four-way coupling effects could be important. On the other hand, the fact that the erosion hole became deeper as the concentration increases (due to the time of exposure being the same) indicated that the expansion of the scar layer could play a key role as well.

The experimental data reported in [22] clearly show a reduction of the integral erosion ratio with the solid mass fraction, which is more significant for case D, where the jet velocity is higher. The two scenarios were numerically reproduced using the mechanistic erosion model, in which the parameter U_{tsh} was 2.0 m/s and the other constants were set as previously reported. The measured and computed relative integral erosion ratios (i.e. after normalization with respect to the value for case D and $C_M = 1\%$) are depicted in Fig. 12(a) as a function of C_M.

The proposed methodology correctly predicted the decrease of the integral erosion ratio with increasing concentration, and this capability appeared mainly attributable to the procedure for estimating the development of the wear profile. The analysis of the time evolution of the maximum wear depth, shown in Fig. 12(b) for case D at different concentrations, gave support to this claim. The deceleration in the development of the erosion hole, almost absent for C_M equal to 1 and 5%, was more and more pronounced for increasing concentration, and, as a consequence, the wear depth increased less

than proportionally with C_M (Fig. 12(c)). This had a clear correspondence with the time evolution of the integral erosion ratio, depicted in Fig. 12(d). For low erosion times the influence of C_M on ER_{int} was practically absent, whilst, as the scar gets deeper, ER_{int} decreased faster for higher C_M.

This means that accounting for the evolution of the wear profile was fundamental for the proposed model to correctly predict the decrease of integral erosion ratio with concentration observed experimentally (Fig. 12(a)). Figure 13 shows, for three values of C_M, the distibutions of the particle impact velocities and angles at $t = 0$ and $t = T$ superimposed to the final erosion depth profiles, and it helps getting insight into this aspect. As the time increased, the particles impact characteristics underwent different evolution histories depending on the solid concentration. In fact, whilst no significant variation was observed for $C_M = 1\%$, a decrease in the impact velocity became more and more enhanced for increasing C_M. This is further highlighted in Fig. 14, which shows the time evolution of the mean particle impact velocity modulus, $\langle |\mathbf{v}_{p,w}| \rangle$. Figure 13 also indicated that the particles experiencing the most reduction of the impact velocity were those traveling through a bigger scar layer before impingement. Time variations in the particle impact angles were apparently less relevant, and, similarly, no change of the number of impingements with time was observed (that is, all particles were able to reach the target wall even for $C_M = 20\%$).

However, it is not correct to conclude that the influence of C_M was limited to that on the extension of the scar layer. A side role was also played by the fact that, as C_M increased, the local average solid volume fraction, Φ, in the scar layer increased as well (Fig. 15). This, in turn, produced changes in

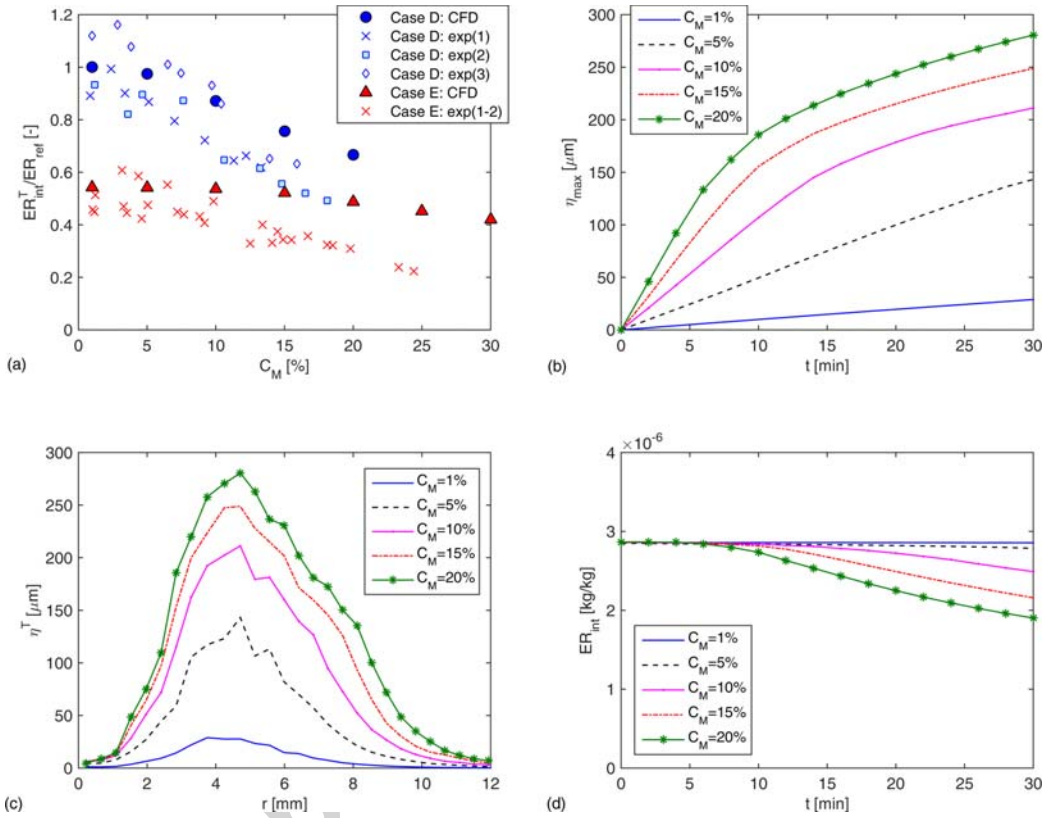

Figure 12: (a) effect of concentration on the integral erosion ratio (normalized by the value for case D at $C_M = 1\%$, referred to as ER_{ref}) for cases E and D: comparison between numerical predictions and experimental data [22]. Labels "exp(1)", "exp(2), and "exp(3)" indicate different repetitions of the experiment; (b) time evolution of the maximum erosion depth for case D at different concentrations; (c) predicted scar depth profiles at the end of the test for for case D at different concentrations; (d) time evolution of the integral erosion ratio for case D at different concentrations.

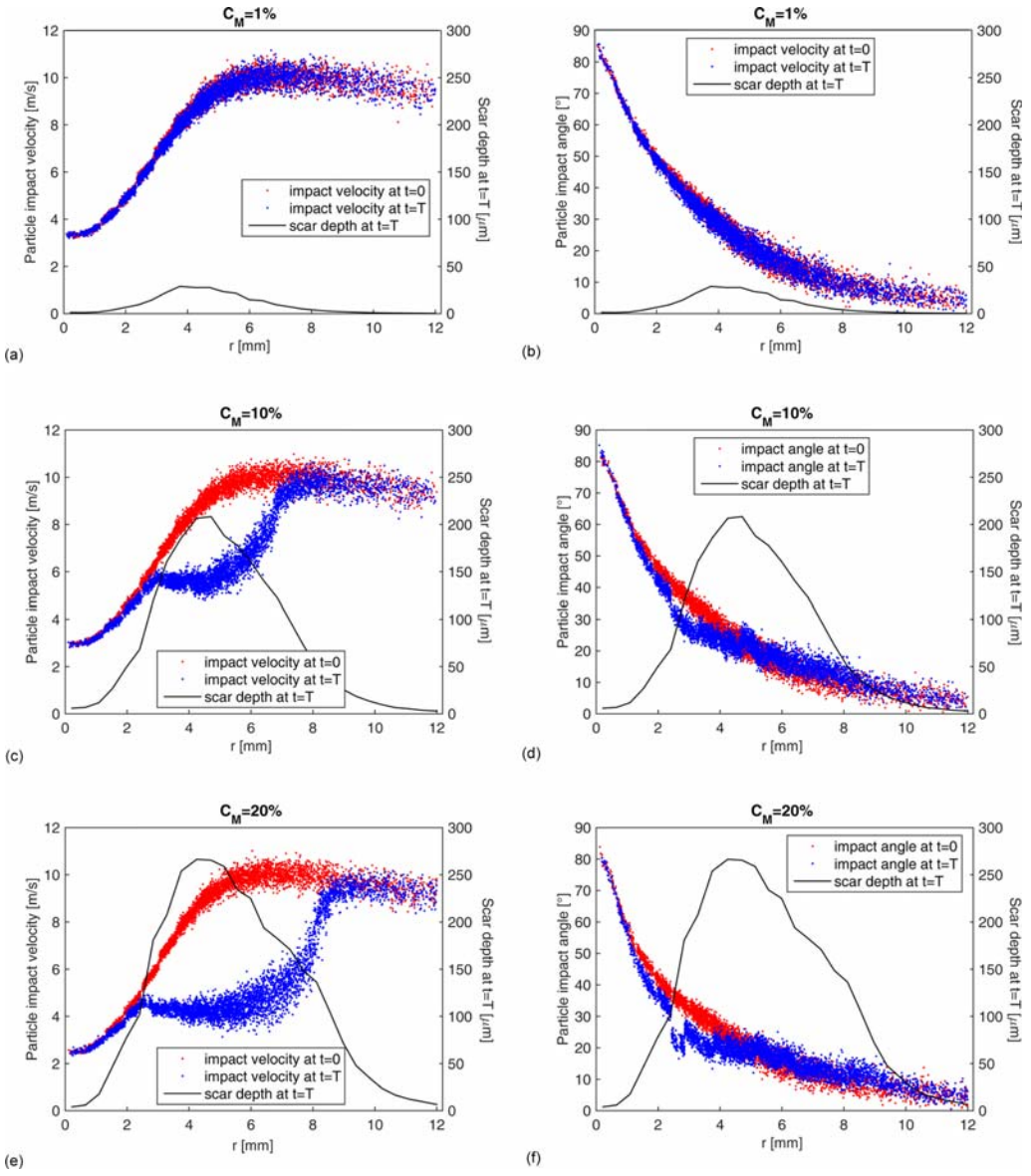

Figure 13: Case D at different concentrations: modulus of the impact velocity (a,c,e) and impact angle (b,d,f) for all tracked particles at $t = 0$ and $t = T$. In all plots, the scar depth at $t = T$ is also shown and labeled on the right side axis.

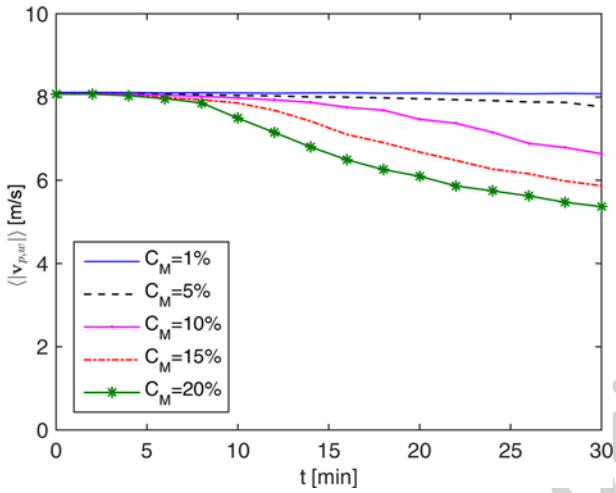

Figure 14: Time evolution of the mean particle impact velocity modulus for case D.

the friction parameter μ_m (Eq. 11), in Re_m (Eq. 10), and, finally, in the drag coefficient C_d (Eq. 8). Thus, the motion of a particle in the scar layer was affected by C_M. Among the fluid dynamic variables solved by the Euler-Euler model, Φ is practically the only one which was strongly affected by C_M. The flow field data for different concentrations of particles were compared, but no detectable change was observed. Thus, the effect of increasing concentration was not strongly related to variations in $\mathbf{U}$ and $\mathbf{V}$.

The experimental data in Fig. 12(a) also indicate that the decrease of the integral erosion ratio with increasing concentration is enhanced for the high-velocity jet. From a qualitatively point of view, this behavior was well captured by the computational model. This capability was mainly attributed to the lower erosion depths occurring in case E (low-velocity jet), which made easier for the particles to cross the scar layer and reach the target wall with almost unchanged velocity.

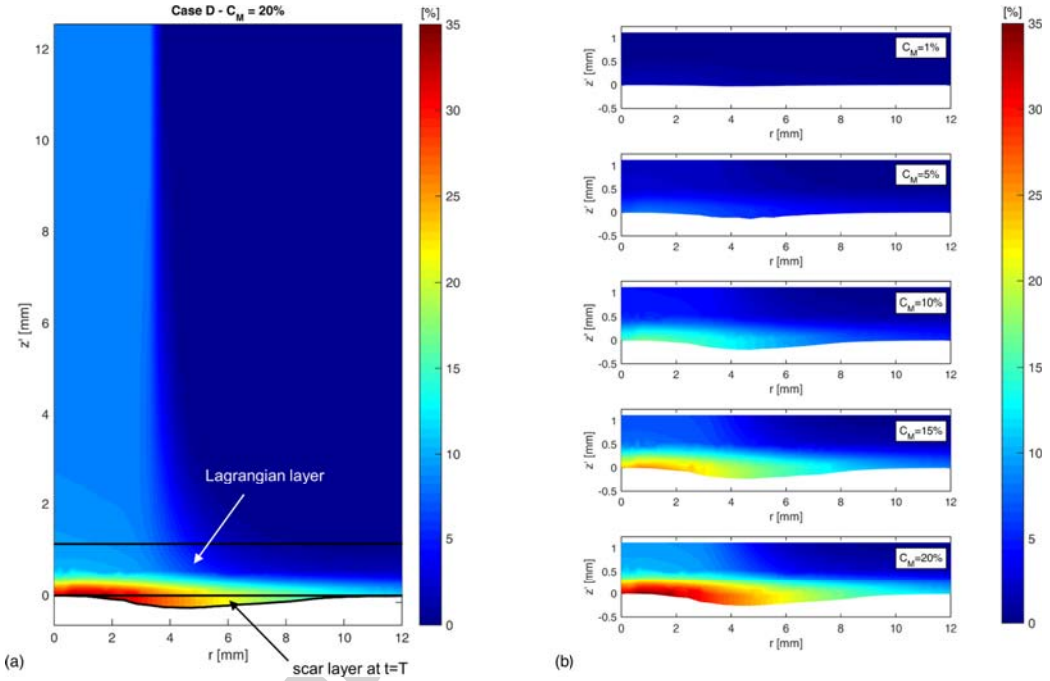

Figure 15: Color plot distribution of the average solid volume fraction at $t = T$ for $C_M = 20\%$, and details of the Φ-distributions within the Lagrangian and scar layer for different values of C_M. The origin of the coordinate z', which is opposite to the z-direction, is at a distance of $d_p/2$ from the uneroded specimen surface.

.

	ER^T_{int} [kg/kg]	
Case	Exp.	CFD
D	$6.04 \cdot 10^{-6}$	$2.83 \cdot 10^{-6}$
E	$3.09 \cdot 10^{-6}$	$1.54 \cdot 10^{-6}$

Table 2: Computed and measured integral erosion ratios for cases D and E at $C_M = 1\%$.

Finally, it is noted that the reduction of the integral erosion ratio with increasing concentration was underestimated by the numerical model. A possible reason is that the μ_m-factor did not allow accurately capturing the already mentioned shielding effect, i.e. the disturbance exerted by the rebounding particles on the incoming ones. Further research work on the Euler-Euler is planned within the authors' research group to improve the prediction accuracy.

4.5. Experiments by Wang et al. [18]

The simulations of the abrasive jet experiments performed by Wang et al. [18] on a 44W carbon steel specimen provided further confirmation to the key role played by the erosion model. As in previous cases D and E, all testing parameters were kept the same except for the solid concentration, which was varied between 1% and 8%. Such an increase of the solid loading was accompanied by a decrease in the integral erosion ratio from $3.21 \cdot 10^{-6}$ to $2.08 \cdot 10^{-6}$ kg/kg.

The experiments were numerically reproduced and, at first, the mechanistic model was employed with the constants suggested by Arabnejad et al. [48] for the most similar material to the 44W carbon steel, that is 1018 carbon steel ($C_1 = 5.90 \cdot 10^{-8}$, $C_2 = 4.25 \cdot 10^{-8}$, and $K = 0.5$). The variable U_{tsh} was

estimated as 2.0 for the 300 μm abrasive particles used in the experiments, and, in the lack of any information on the shape of the grains, F_s and ψ were set as 0.53 and 0.76, respectively.

However, these settings were not appropriate for this case, yielding not only significant underestimation of the integral erosion ratio but also the same integral erosion ratio for the different values of C_M, in clear contradiction with the experimental evidence (Fig. 16). The numerical results can be interpreted with the aid of plots (a,c,e) in Fig. 17, which indicate that the maximum wear depth linearly increased with time, that the scar depth increased proportionally with C_M, and that the integral erosion ratio did not change over time. These findings suggested that the wear depths predicted by the mechanistic erosion model with the constants for 1018 carbon steel were too small for any significant deceleration of the particles in the scar layer to take place even for the highest concentration.

With the aim of assessing this interpretation, the constants C_1 and C_2 of the erosion model were increased to $3.54 \cdot 10^{-7}$ and $2.55 \cdot 10^{-7}$, respectively, so that the predicted ER_{int}^{T} at $C_M = 1\%$ became equal to the experimental value. This change affected the penetration rate, which reduced in time (Fig. 17(b)), yielding a temporal decrease of the integral erosion ratio (Fig. 17(f)). As already discussed in section 4.4, this phenomenon was enhanced for higher C_M, because the particles encountered more resistance to motion and they had to travel a longer distance before reaching the target wall. This caused the wear profile to develop less than proportionally with C_M (Fig. 17(e)), and, thus, it produced a decreasing trend of integral erosion ratio with C_M (Fig. 16), in good agreement with the laboratory experiment.

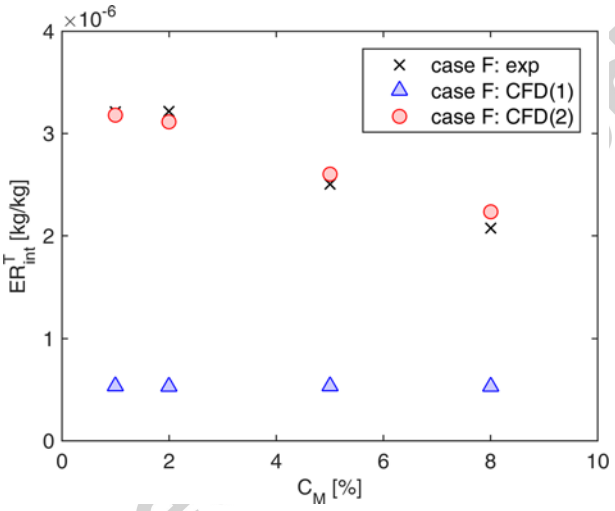

Figure 16: Case F: effect of concentration on the integral erosion ratio as measured by Wang et al. [18] and predicted by our CFD simulations. In series CFD(1), the constants C_1 and C_2 in the mechanistic erosion model were those recommended for 1018 carbon steel, whilst in CFD(2), their values were $3.54 \cdot 10^{-7}$ and $2.55 \cdot 10^{-7}$.

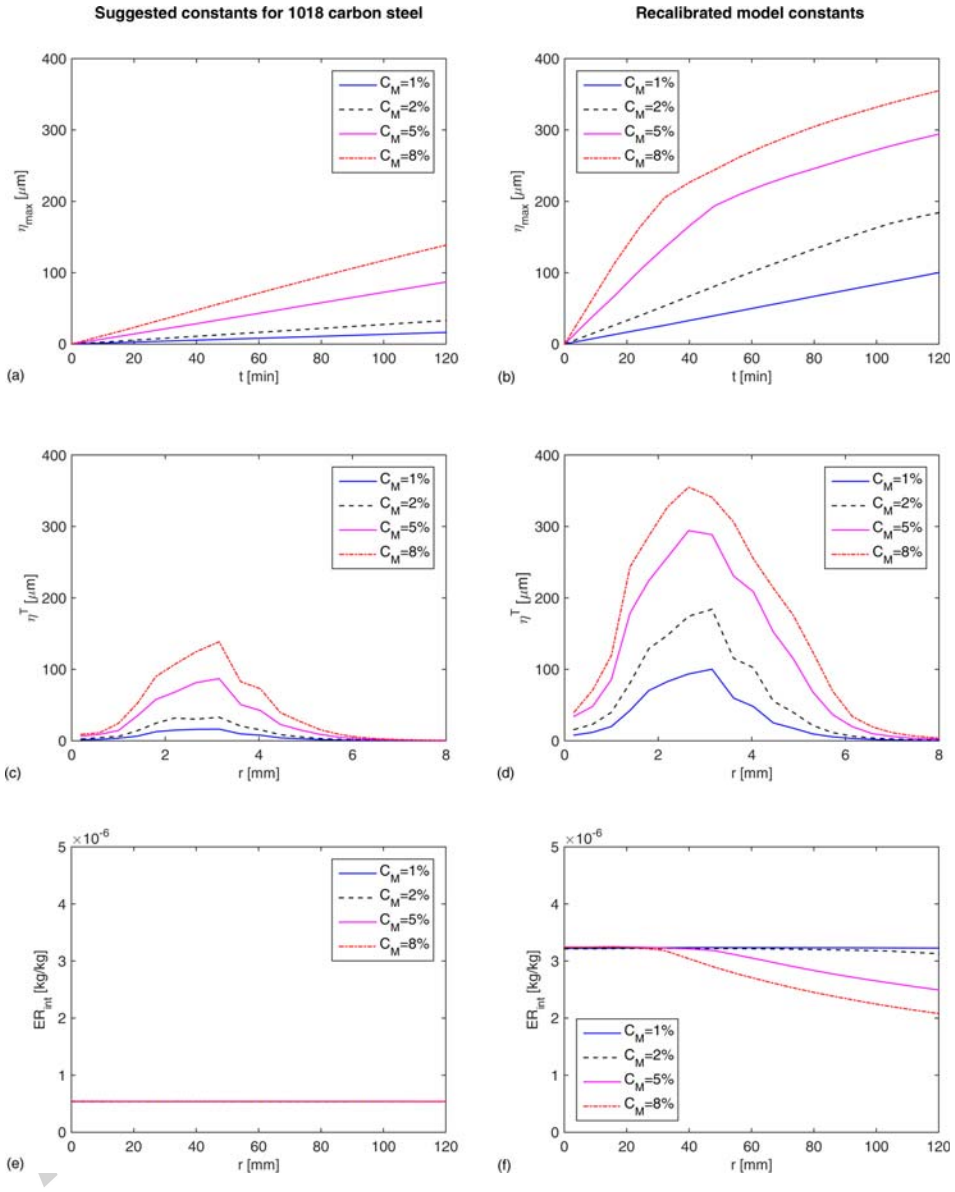

Figure 17: Numerical results for case F at different C_M: (a,b) time evolution of the maximum erosion depth; (c,d) wear profile at the end of the test; (e,f) time evolution of the integral erosion ratio. In plots (a,c,e), the constants C_1 and C_2 in the mechanistic erosion model were those recommended for 1018 carbon steel, whilst in plots (b,d,f) their values were $3.54 \cdot 10^{-7}$ and $2.55 \cdot 10^{-7}$.

5. Discussion

Some considerations on the numerical results are now presented, and future research directions for further developments are outlined.

5.1. Importance of the dynamic evolution algorithm

The decrease of the integral erosion ratio with increasing concentration was achieved through a two-phase model which accounts for the complex phenomena occurring in dense flows and a post-processing procedure which dynamically updates the wear profile. Figure 18 indicates that the unsteady treatment of the wear process was necessary for the model to correctly capture the effect of the amount of particles in the jet. However, from these results it cannot be concluded that the decrease of integral erosion ratio with increasing concentration observed in many experiments is due to geometry changes and not to the shielding effect. In fact, the particle tracking in the Lagrangian and scar layers (and thus the evolution of the wear profile) was indeed affected by concentration through the parameter μ_m. In turn, μ_m has some relation with the interactions occurring in dense slurries but, like any of the other terms in the Euler-Euler equations, is not specifically associated to particle-particle collisions and contacts. Future research will be aimed at isolating the effect of particle-particle interactions in the Euler-Euler model and within the particle tracking in the erosion hole. This will yield an improved version of the proposed methodology, which will be capable in assessing the importance of the shielding effect.

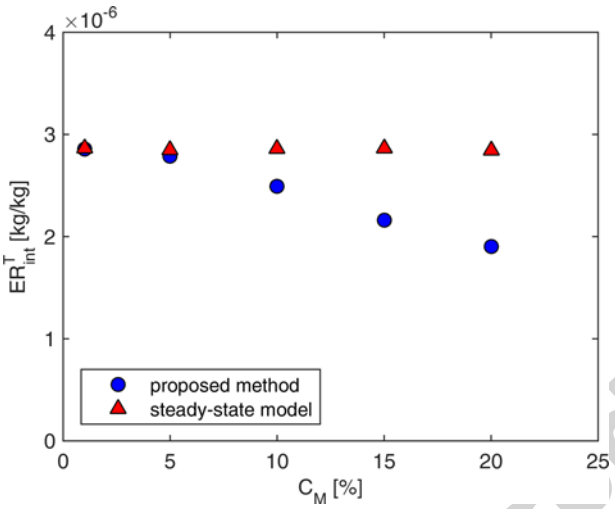

Figure 18: Integral erosion ratio at $t = T$ as a function of concentration for case C: comparison between the proposed method and a steady-state model.

5.2. Assumptions on the particle size distribution

The Euler-Euler models solve for just one solid phase, which is characterized by a single-particle size. Thus, in this work, the solid phase was treated as monodisperse with representative size equal to the mean diameter. In reality, the particles used in the experiments are never monodisperse, and, therefore, this simplification could have affected the validation results [56].

To have a broad idea of the influence that the approximation of monodisperse particles had on the numerical predictions, case A was simulated with particle size equal to the min/max values indicated by the experimenter [23], namely 125 μm and 180 μm, and the wear estimates were compared with that previously obtained considering the mean diameter, that is 150 μm. The results, shown in Fig. 19, indicated that the time evolution of the integral erosion ratio was indeed affected by particle size, and, particularly,

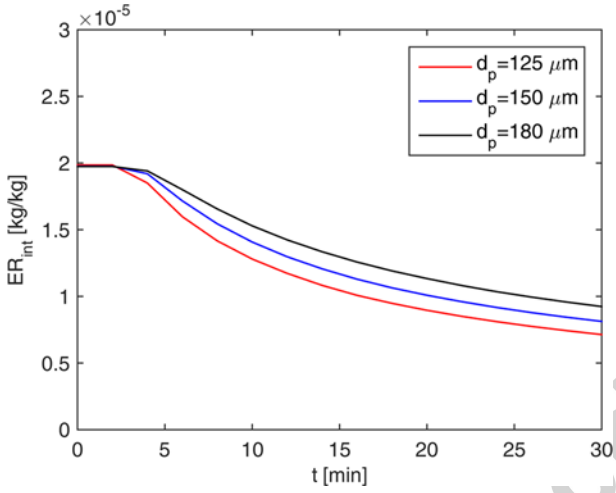

Figure 19: Time evolution of the integral erosion ratio for case A: effect of particle size.

bigger particles determined a slower decrease of the integral erosion ratio. This was interpreted because of the fact that bigger particles possess greater inertia, and, therefore, they were more prone to cross the scar layer with constant velocity. The plot also reveals that the steady state integral erosion ratio (that is, the value at the end of the first timestep) was substantially unaffected by the particle size. This was attributed to the fact that the used erosion model (Eqs. 12-14) does not involve an explicit dependence on the particle size, which has only a minor influence via the threshold velocity, U_{tsh}, in the deformation wear term.

In order to account for polydisperse particle distributions, the Euler-Euler model should be turned into an Eulerian multi-fluid model, which can solve for different particle size classes. This will open challenging perspectives for future development of the current research.

5.3. Sources of uncertainty in experiments and simulation

It is well known that every time a comparison is made between experiments and numerical predictions, the uncertainties inherent in both approaches must be taken into account.

Sources of uncertainty in the experimental data include measurement errors, errors in the positioning of the specimen, and difficulties in keeping the experimental conditions constant during the test. Regarding the last aspect, it is noted that all the tests considered for comparison were performed in setups where the particles are recirculated. The recycle use of the abradant may have induced spurious effects due to possible changes in particle size and shape [23, 57]. Another key point was the evaluation of the particle concentration. Mansouri et al. [37] and Mahdavi et al. [22] showed that the solid concentration coming out from the nozzle is different than the prepared concentration which is added to the slurry tank, but Nguyen et al. [23] and Wang et al. [18] did not specify how they measured this parameter. Furthermore, the slurry concentration could also have varied during the tests. The azimuthal variability of the radial depth profile observed in Fig. 11 and the difference between the experimental series in Fig. 12 may be interpreted in the light of the considerations set out above. Unfortunately, not enough information was available to the authors to attribute error bars to the data.

The numerical erosion predictions were subjected to many uncertainties as well, as they were obtained as output of a complex process involving an Euler-Euler simulation, the tracking of particle trajectories, and the application of an erosion model. All these steps included factors of uncertain nature or difficult to obtain, which may affect the wear estimates. Neverthe-

less, quantifying their combined effects in realistic error bars was extremely complicated. The experience gained in previous research was fundamental to assign appropriate values to these subjectively determined parameters.

5.4. Comparison with alternative approaches

Finally, the present method is discussed in the light of some of the alternative approaches illustrated in Section 1. First, the procedure for estimating the time evolution of the surface profile would reduce to the particle-only model by Solnordal and Wong [32] if the inertia of the particles in the scar layer was dominant and the effect of the surrounding slurry was negligible. Under this condition, in fact, the particles would keep the same velocity across the scar layer, and the nonlinear growth of the erosion hole would be due only to changes in the impact locations and angles. Second, the combination of a CFD simulation with uneroded geometry and a simplified modeling of the flow within the erosion hole is a feature shared with the model of Kowsari [27] for application to ASJM. Compared to [27], the assumptions of the proposed method on the flow in the erosion hole were, on one hand, more simplistic, but, on the other hand, they did not require experimental calibration. Third, the approach of Rizkalla and Fletcher [35] appears conceptually simpler, as it does not introduce a Lagrangian layer, and it allows for a more physically based description of the unsteady process. At time same time, it requires higher simulation time, and it strongly relies on the predicted solid phase velocity in the near-wall cells, which, in the absence of a well-established wall boundary conditions for the solid phase, may be hard to estimate accurately.

5.5. Note on the computational gain

For all the simulations performed in this study, the overall calculation time (including the solution of the Eulerian-Eulerian equations and the erosion prediction with updating geometry) was less than one hour on a computer with Intel Core i7-4790 CPU at 3.60 GHz and 8 GB RAM. The time saving over one-way and two-way coupled Eulerian-Lagrangian simulations, in which the particles are tracked in the whole computational domain, was estimated as -67% and -90%, respectively. To obtain these values, the simulation time of the steady-state Eulerian-Lagrangian simulations (performed on the same 2D axi-symmetrical domain discretized with the same number of cells) was multiplied by a factor equal to the number of timesteps, i.e. 15. The computational gain would be even higher if compared to more detailed two-phase models, like those accounting for particle-particle interactions or those in which the particles are fully resolved in space. This further enhances the potential of the proposed method for applications involving complex flows.

6. Conclusion

A new computational strategy was developed for estimating the impact erosion produced by liquid-solid slurries. The method required to perform just one steady-state simulation of the slurry flow by an Euler-Euler model, followed by an iterative post-processing procedure. Particularly, use was made of the Euler-Euler model developed within the authors' research group [40], which extensive past research proved to be computationally efficient and effective in capturing the effect of the complex interactions occurring

in slurry flows. A small Lagrangian layer was defined adjacent to the solid boundaries, in which the trajectories of Lagrangian particles were tracked and a single-particle erosion model was applied to each particle-wall impingement, determining the formation of an erosion hole. The particle tracking and the update of the wear profile were iteratively executed in a time loop. The slurry flow field in the erosion hole was obtained by an approximate model, thereby avoiding the need of repeating the Euler-Euler simulation at every time step. Besides the Euler-Euler model, also the particle equation of motion accounted for the effect of the presence of multiple particles in the slurry mixture via empirical parameters.

The capability of the method was assessed by reproducing several slurry abrasive jet experiments reported in the literature [18, 22, 23, 37]. The model proved able to reproduce the deceleration of the erosion process which is well known to accompany the increase in the erosion depth. Furthermore, it allowed capturing the decrease in the integral erosion ratio with increasing concentration.

The method provided improved wear predictions compared to the CFD-based erosion prediction models commonly used in the engineering practice. The concept underlying the proposed strategy has thus potential for effectively addressing geometries of engineering interest, which cannot be practically simulated using more complex models that accurately describe all the physical mechanisms at the basis of the slurry transport and erosion processes, because their computational burden would be unaffordable. This makes the method worthy of application to real case studies and, at the same time, of further research and improvement.

Acknowledgments

Authors would like to acknowledge Soroor Karimi from the E/CRC at the University of Tulsa for sending us her paper [22].

References

[1] R.W. Lyczkowski, J.X. Bouillard, State-of-the-art review of erosion modeling in fluid/solid systems, Prog. Energy Comb. Sci. 28 (2002), 543–602.

[2] M. Parsi, K. Najmi, F. Najafifard, S. Hassani, B.S. McLaury, S.A. Shirazi, A comprehensive review of solid particle erosion modeling for oil and gas wells and pipelines applications, J. Nat. Gas Sci. Eng. 21 (2014), 850–873.

[3] S. Elghobashi, On predicting particle-laden turbulent flows, Appl. Sci. Res. 52 (1994), 309–329.

[4] G.V. Messa, S. Malavasi, The effect of sub-models and parameterizations in the simulation of abrasive jet impingement tests, Wear 370-371 (2017), 59–72.

[5] L. Nøkleberg, T. Søntveg, Erosion of oil&gas choke valves using computational fluid dynamics and experiment, Int. J. Heat Fluid Flow 19 (1998), 636–643.

[6] A. Forder, M. Thew, D. Harrison, A numerical investigation of solid particle erosion experienced within oilfield control valves, Wear 216 (1998), 184–193.

[7] M.S. Wallace, W.M. Dempster, T. Scanlon, J. Peters, S. McCulloch, Prediction of impact erosion in valve geometries, Wear 256 (2004), 927–936.

[8] L. Guomei, W. Yueshe, H. Renyang, C. Xuewen, L. Changzhi, M. Tao, Numerical simulation of predicting and reducing solid particle erosion of solid-liquid two-phase flow in a choke, Pet. Sci. 6 (2009), 91–97.

[9] E. Gharaibah, Y. Zhang, R. Paggiaro, J. Friedemann, Prediction of Sand Erosion in Choke Valves CFD Model Development and Validation against Experiments, in: Proceedings of the OTC 2013, Paper No. OTC24271, 2013.

[10] Z. Lin, X.D. Ruan, Z.C. Zhu, X. Fu, Three dimensional numerical investigation of solid particle erosion in gate valves, Proc. IMechE Part C 228 (2014), 1670–1679.

[11] H. Zhu, Q. Pan, W. Zhang, G. Feng, X. Li, CFD simulations of flow erosion and flow-induced deformation of needle valve: Effects of operation, structure and fluid parameters, Nucl. Eng. Des. 273 (2014), 396–411.

[12] G.V. Messa, Y. Wang, S. Malavasi, Estimation of the useful lifetime of a gate valve subjected to impact erosion, in: Proceedings of AIMETA XXIII Conference, 1 (2017), 147–163.

[13] C.T. Crowe, J.D. Schwarzkopf, M. Sommerfeld, Y. Tsuji, Multiphase Flows with Droplets and Particles, CRC Press, Boca Raton, US-FL, 2012.

[14] V.B. Nguyen, Q.B. Nguyen, Y.W. Zhang, C.Y.H. Lim, B.C. Khoo, Effect of particle size on erosion characteristics, Wear 348-349 (2016), 126–137.

[15] C.A.R. Duarte, F.J. de Souza, Innovative pipe wall design to mitigate elbow erosion: A CFD analysis, Wear 380 (2017), 176–190.

[16] S. Turenne, M. Fiset, J. Masounave, The effect of sand concentration on the erosion of materials by a slurry jet, Wear 133 (1989), 95–106.

[17] I. Kleis, D. Kulu, Solid particle erosion. Occurrence, prediction and control, Springer-Verlag, London UK, 2008.

[18] M.H. Wang, C. Huang, K. Nandakumar, P. Minev, J. Luo, S. Chiovelli, Computational fluid dynamics modelling and experimental study of erosion in slurry jet flows, Int. J. Comput. Fluid Dyn. 23 (2009), 155-172.

[19] T. Frosell, M. Fripp, E. Gutmark, Investigation of slurry concentration effects on solid particle erosion rate for an impinging jet, Wear 342-343 (2015), 33–43.

[20] H.S. Grewal, H. Singh, E.S. Yoon, Interplay between erodent concentration and impingement angle for erosion in dilute water-sand flows, Wear 332-333 (2015), 1111–1119.

[21] A. Mansouri, M. Mahdavi, S.A. Shirazi, B.S. McLaury, Investigating the Effect of Sand Concentration on Erosion Rate in Slurry Flows, in: Proceedings of NACE Corrosion 2015 International Congress & Expo, Paper No. 6130, 2015.

[22] M. Mahdavi, S. Karimi, S.A. Shirazi, B.S. McLaury, Parametric study of erosion under high concentrated slurry: experimental and numerical analyses, in: Proceedings of the ASME-FEDSM 2016, Paper No. 7718, 2016.

[23] V.B. Nguyen, Q.B. Nguyen, Z.G. Liu, S.Wan, C.Y.H. Lim, Y.W. Zhang, A combined numerical experimental study on the effect of surface evolution on the water sand multiphase flow characteristics and the material erosion behavior, Wear 319 (2014), 96–109.

[24] H. Nouraei, K. Kowsari, J.K. Spelt, M. Papini, Surface evolution models for abrasive slurry jet micro-machining of channels and holes in glass, Wear 309 (2014), 65–73.

[25] N. Haghbin, J.K. Spelt, M. Papini, Abrasive waterjet micro-machining of channels in metals: comparison between machining in air and submerged in water, Int. J. Mach. Tools Manuf. 88 (2015), 108–117.

[26] N. Haghbin, J.K. Spelt, M. Papini, Abrasive waterjet micro-machining of channels in metals: model to predict high aspect-ratio channel profiles for submerged and unsubmerged machining, J. Mater. Process. Technol. 222 (2015), 399–409.

[27] K. Kowsari, H. Nouraei, B. Samareh, M. Papini, J.K. Spelt, CFD-aided prediction of the shape of abrasive slurry jet micro-machined channels in sintered ceramics, Ceram. Int. 42 (2016), 7030–7042.

[28] K. Kowsari, M.R. Sookhaklari, H. Nouraei, M. Papini, J.K. Spelt, Hybrid erosive jet micro-milling of sintered ceramic wafers with and with-

out copper-filled through holes, J. Mater. Process. Technol. 230 (2016), 198–210.

[29] B.S. McLaury, S.A. Shirazi, T.L. Burden, Effect of entrance shape on erosion in the throat of chokes, J. Energ. Resour-ASME 122 (2000), 198–204.

[30] C.Y. Wong, C.B. Solnordal, J. Wu, CFD modeling and experimental observations of changing surface profiles caused by solid-particle erosion, SPE Production and Operations 29 (2014), 69–74.

[31] A. Ghobeity, T. Krajac, T. Burzynski, M. Papini, J.K. Spelt, Surface evolution models in abrasive jet micromachining, Wear 264 (2008), 185–198.

[32] C.B. Solnordal, C.Y. Wong, Predicting surface profile evolution caused by solid particle erosion, in: Proceedings of the Ninth International Conference on CFD in the Minerals and Process Industries CSIRO, 2012.

[33] M. Schrade, S. Staudacher, M. Voigt, Experimental and numerical investigation of erosive change of shape for high-pressure compressors, in: Proceedings of the ASME Turbo Expo 2015, 2015. Paper No. GT2015-42061.

[34] Y. Yaobao, Y. Jiayang, G. Shengrong, Numerical study of solid particle erosion in hydraulic spool valves, Wear 392–393 (2017), 174–189.

[35] P. Rizkalla, D.F. Fletcher, Development of a slurry abrasion model using an Eulerian-Eulerian “two-fluid” approach, Appl. Math. Mod. 44 (2017), 107–123.

[36] G.V. Messa, S. Malavasi, A numerical strategy to account for the effect of self-induced geometry changes in wear estimation, in: Proceedings of the 9th International Conference on Multiphase Flow, Paper No. 133, 2016.

[37] A. Mansouri, S.A. Shirazi, B.S. McLaury, Experimental and numerical investigation of the effect of viscosity and particle size on the erosion damage caused by solid particles, in: Proceedings of the ASME-FEDSM 2014, Paper No. 21613, 2014.

[38] D.B. Spalding, Numerical Computation of Multi-Phase Fluid Flow and Heat Transfer, in: C. Taylor, K. Morgan (Eds.), Prineridge Press Limited, Swansea, UK, 1980, pp. 139–168.

[39] G.V. Messa, M. Malin, S. Malavasi, Numerical prediction of pressure gradient of slurry flows in horizontal pipes, in: Proceedings of the ASME-PVP 2013, Paper No. 97460, 2013.

[40] G.V. Messa, S. Malavasi, Improvements in the numerical prediction of fully-suspended slurry flow in horizontal pipes, Powder Technol. 270 (2015), 358–367.

[41] A. Haider, O. Levenspiel, Drag coefficient and terminal velocity of spherical and nonspherical particles, Powder Technol. 58 (1989), 63-70.

[42] N.S. Cheng, A.W.K. Law, Exponential formula for computing effective viscosity, Powder Technol. 129 (13) (2003) 156-160.

[43] V. Yakhot, S.A. Orszag, S. Thangam, T.B. Gatski, C.G. Speziale, Development of turbulence models for shear flows by a double expansion technique. Phys. Fluids A, 4(7) (1992), 1510–1520.

[44] J.C. Ludwig, PHOENICS On Line Information System, Concentration, Heat and Momentum Limited (CHAM), London, 2004. http://www.cham.co.uk/phoenics/d_polis/polis.htm

[45] R.I. Issa, P.J. Oliveira, Assessment of a particleturbulence interaction model in conjunction with an Eulerian two-phase flow formulation, in: Proceedings of the 2nd International Symposium on Turbulence Heat and Mass Transfer, 1997, pp. 759-770.

[46] G.V. Messa, S. Malavasi, Numerical prediction of particle distribution of solid-liquid slurries in straight pipes and bends, Eng. Appl. Comput. Fluid Mech., 8(3) (2014), 356–372.

[47] H. Arabnejad, A. Mansouri, S.A. Shirazi, B.S. McLaury, Development of mechanistic erosion equation for solid particles, Wear 332-333 (2015), 1044-1050.

[48] H. Arabnejad, A. Mansouri, S.A. Shirazi, B.S. McLaury, Evaluation of solid particle erosion equations and models for oil and gas industry applications, in: Proceedings of the SPE Annual Technical Conference and Exhibition, 2015, Paper No. SPE-174987-MS.

[49] H. Arabnejad, A. Mansouri, S.A. Shirazi, B.S. McLaury, Abrasion erosion modeling in particulate flow, Wear 376-377 (2017), 1194-1199.

[50] B.S. McLaury, S.A. Shirazi, An alternative method to API RP 14E for predicting solids erosion in multiphase flow, ASME J Energy Resour Technol, 122 (2000), 115-122.

[51] A.L. Ferre, C.A. Shook, Coarse particle wall friction in vertical slurry flows, Particul. Sci. Tech. 16 (1998), 125–133.

[52] G.V. Messa, G. Ferrarese, S. Malavasi, A mixed Euler-Euler/Euler-Lagrange approach to erosion prediction, Wear 342-343 (2015), 138–153.

[53] C.T. Crowe, M.P. Sharma, D.E. Stock, The Particle-Source-In Cell (PSI-CELL) model for gas-droplet flows, J. Fluids Eng., 99 (1977), 325–332.

[54] S. Karimi, S.A. Shirazi, B.S. McLaury, Predicting fine particle erosion utilizing computational fluid dynamics, Wear, 376-377 (2017), 1130–1137.

[55] R. Picardi, L. Zhao, F. Battaglia, On the ideal grid resolution for two-dimensional eulerian modeling of gas-liquid flows, ASME J. Fluids Eng, 178 (2016), No. 114503.

[56] C. Solnordal, L. Graham, G. Short, C. Wong, J. Wu, Determination of erosion rate characteristics for particles of different sizes suspended in liquid, in: Proceedings of the 20th Int. Conf. Hydrotransport, 2017, 183–195.

[57] H. McI. Clark, Particle velocity and size effects in laboratory slurry erosion measurements OR... do you know what your particles are doing? Tribol Int, 35 (2002), 617–624.